

₁ Physics-Infused Reduced-Order Modeling for Analysis of
₂ Ablating Hypersonic Thermal Protection Systems

₃

₄ November 25, 2025

₅

Abstract

This work presents a *physics-infused reduced-order modeling* (PIROM) framework towards design, analysis, and optimization of non-decomposing ablating hypersonic thermal protection systems (TPS), and is demonstrated via the modeling of transient thermo-ablative responses of multi-layered hypersonic TPS. The PIROM architecture integrates a reduced-physics backbone, based on the lumped-capacitance model (LCM) and a surface recession model (SRM), with data-driven correction dynamics formulated via a coarse-graining approach rooted in the Mori-Zwanzig formalism. The LCM is coupled to the SRM to capture the one-dimensional surface recession of the ablating TPS as a function of the surface temperature. While the LCM and SRM capture the dominant physics of the ablating TPS response, the correction terms compensate for residual dynamics arising from higher-order non-linear interactions and temperature-advection effects due to surface recession. The PIROM consistently achieves errors of $\approx 0.5\%$ for a wide range of extrapolative settings of design parameters involving time-and-space varying boundary conditions and SRM models, and improves by an order of magnitude by the LCM alone. Moreover, the PIROM delivers online evaluations that are two orders of magnitude faster than the full-order model (FOM). These results demonstrate that PIROM effectively reconciles the trade-offs between accuracy, generalizability, and efficiency, providing a promising framework for optimizing multi-physical dynamical systems, such as TPS, under diverse operating conditions.

₂₅

1 Introduction

₂₆ At hypersonic speeds, aerospace vehicles experience extreme aero-thermo-dynamic environments that require specialized thermal protection systems (TPS) to shield internal sub-
₂₇ structures, electronics, and possibly crew members from the intense aerodynamic heating.
₂₈ The TPS is composed of ablating materials to withstand the high-energy physics – a high-
₂₉ temperature capable fibrous material injected with a resin that fills the pore network and
₃₀ strengthens the composite [1]. The TPS design promotes the exchange of mass through
₃₁ thermal and chemical reactions (i.e., ablation), effectively mitigating heat transfer to the
₃₂ sub-structures. As a result, accurate prediction for the ablating TPS response under ex-
₃₃ treme hypersonic heating becomes critical to ensuring survivability, performance, and safety
₃₄ of hypersonic vehicles. Not only is it necessary to assess the performance of the thermal
₃₅ environment, but also to ensure the integrity of the vehicle's structure and systems under extreme

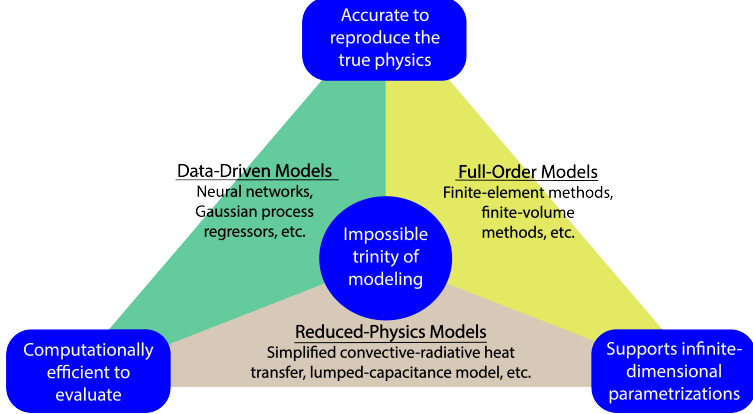


Figure 1: The impossible trinity of modeling: accuracy, generalizability, and efficiency.

management systems, but also the shape changes of the vehicle’s outer surface induced by the ablating material, and its impact on the aerodynamics, structural integrity, and controllability.

Even with today’s advancements in computational resources and numerical methods, high-fidelity simulations of ablating TPS remains a formidable challenge, both theoretically and computationally. On the theoretical side, the thermo-chemical reactions, coupled with the irregular pore network structure and ablating boundaries, translate into complex non-linear equations governing multi-physical interactions across several spatio-temporal scales [1, 8]. On the computational side, numerical approaches based on finite-element (FEM) or finite-volume (FVM) methods yield systems of differential equations modeling the transient thermo-ablative response of the TPS [5]. The FEM discretizations lead to high-dimensional systems of equations, resulting in prohibitive computational costs for many-query applications such as design, optimization, uncertainty quantification, and real-time applications, where possibly thousands of model evaluations are required.

Reduced-order models (ROMs) have emerged as a promising approach to alleviate the computational costs of high-fidelity simulations [6, 11]. Ideally, a ROM should be: (1) accurate to reproduce high-fidelity solutions, (2) support continuous or infinite-dimensional design parameters such as geometrical shapes and material distributions, (3) be computationally efficient to evaluate to allow for fast turnaround times in design optimization. However, the above three capabilities usually form an *impossible trinity of modeling*, as illustrated in Fig. 1; building a ROM that achieves any two capabilities sacrifices the third.

The impossible trinity poses a significant challenge in the development of ROMs for the multi-disciplinary transient analysis and optimization of ablating TPS. Specifically, full-order models (FOMs), e.g., FEMs or FVMs, offer high accuracy and robust generalization over design spaces, but are computationally expensive to evaluate. Reduced-physics models (RPMs) – such as simplified convective-radiative heat transfer or engineering correlations – are low-dimensional models that achieve efficiency and broad applicability by ignoring higher-order non-linear effects. However, RPMs sacrifice accuracy for complex thermo-ablative responses due to the simplifications and assumptions inherent in their formulation, and it is generally not clear how to systematically leverage existing high-fidelity data to improve RPMs [18].

67 Lastly, data-driven ROMs, such as Gaussian Process Regression (GPR) [?], Neural Net-
68 works (NNs), and neural ordinary differential equations (NODEs) [3], can provide accurate
69 and computationally-efficient approximations of high-fidelity models for complex thermo-
70 ablative responses. However, these data-centric approaches often demand extensive high-
71 fidelity data for training, do not necessarily satisfy fundamental physical constraints or con-
72 servation laws, and thus do not generalize well to the design spaces outside the training [16].

73 This work presents the extension of the *physics-infused reduced-order modeling* (PIROM)
74 framework to include effects of ablation for TPS applications, previously ignored in Ref. [17].
75 Specifically, the PIROM is demonstrated for the transient thermo-ablative response of multi-
76 layered hypersonic TPS. The PIROM is a non-intrusive framework that combines the strengths
77 of physics-based models with machine learning to formulate and train ROMs for parametrized
78 non-linear dynamical systems. The backbone of the PIROM is the physics-based component,
79 i.e., the RPM, which in this work is composed of: (1) a *lumped capacitance model* (LCM)
80 to model the average heat transfer within the TPS layers, and (2) a *surface recession model*
81 (SRM) to model one-dimensional surface ablation.

82 Leveraging the *Mori-Zwanzig* (MZ) formalism [15, 14, 13], the RPM is rigorously ex-
83 tended with data-driven hidden dynamics to account for the missing physics in the LCM,
84 which are learned from high-fidelity data. The hidden dynamics enable higher predictive
85 accuracy of the PIROM when subjected to complex boundary conditions and SRM model
86 variations. For the TPS problem, the MZ approach produces a sufficiently simple model
87 form while maintaining the physical consistency of the PIROM, as well as the dependence
88 on design parameters. Thus, the PIROM aims to solve the ITM by leveraging the gen-
89 eralizability and computational efficiency of RPMs, while incorporating the accuracy and
90 adaptability of data-driven extensions. More importantly, the PIROM formulation provides
91 a general methodology for developing PIROMs for other multi-physics problems.

92 The specific objectives of this work are summarized as follows:

- 93 1. Extend the previous PIROM formulation in Ref. [17] to model transient thermo-
94 ablative response of multi-layered hypersonic TPS through a systematic coarse-graining
95 procedure based on the Mori-Zwanzig formalism.
- 96 2. Benchmark the accuracy, generalizability, and computational accelerations of the PIROM
97 against the RPM and the high-fidelity FEM solutions of ablating TPS, thus quanti-
98 fying the PIROM’s capabilities to solve the ITM in complex multi-physical non-linear
99 dynamical systems.

100 2 Modeling of Thermal Protection Systems

101 This section presents the problem of modeling the transient thermo-ablative response of a
102 non-decomposing TPS, subjected to extreme hypersonic heating. Two different but math-
103 ematically connected solution strategies are provided: (1) a high-fidelity full-order model
104 (FOM) based on a finite element method (FEM), and (2) a RPM based on a *lumped ca-*
105 *pacitance model* (LCM) and a one-dimensional *surface recession model* (SRM). The FOM is
106 computationally expensive but provides the highest fidelity, while the RPM is computa-
107 tionally efficient but has low predictive fidelity. However, both models are physically consistent

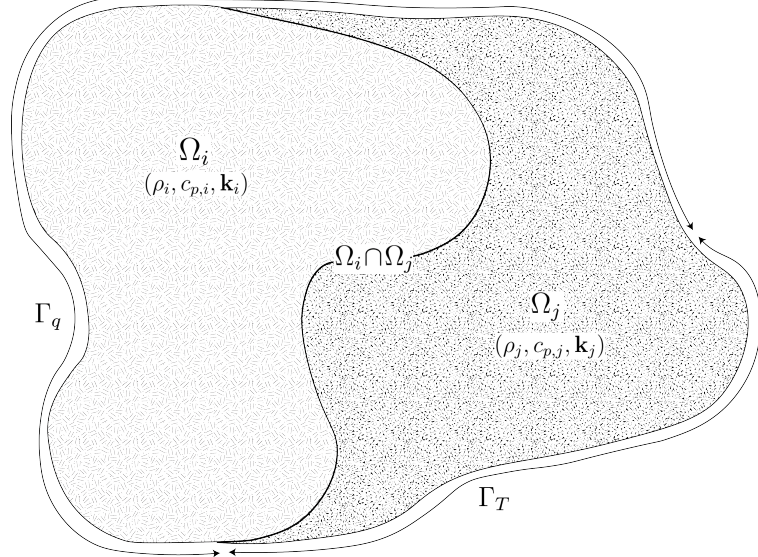


Figure 2: General domain Ω with prescribed Neumann and Dirichlet boundary conditions on Γ_q and Γ_T . Mesh displacement $w(x, t)$ occurs on the Γ_q boundary.

108 to high-dimensional design variables. The following discussion presents the TPS modeling
109 problem and the FOM and RPM solution strategies.

110 2.1 Governing Equations

111 The multi-physics for a non-decomposing ablating TPS involves the *energy equation*, which
112 captures the transient heat conduction inside the TPS, and the *pseudo-elasticity equation*,
113 which models the transient mesh motion due to surface recession. The governing PDEs are
114 described as follows.

115 2.1.1 Energy Equation

116 Consider a generic domain $\Omega \subset \mathbb{R}^{d=2}$ or 3 , illustrated in Fig. 2. Let $\partial\Omega = \Gamma_q \cup \Gamma_T$ and
117 $\Gamma_q \cap \Gamma_T = \emptyset$, where a Neumann $q_b(x, t)$ boundary condition is prescribed on the Γ_q boundary,
118 and represents the surface exposed to the hypersonic boundary layer. The Dirichlet $T_b(x, t)$
119 boundary condition is prescribed on the boundary Γ_T . The TPS is divided into N non-
120 overlapping components $\{\Omega_i\}_{i=1}^N$, as illustrated in Fig. 2 for $N = 2$. The i -th component Ω_i is
121 associated with material properties $(\rho_i, c_{p,i}, \mathbf{k}_i)$, which are continuous within one component,
122 and can be discontinuous across two neighboring components.

123 The energy equation describes the transient heat conduction,

$$\rho c_p \left(\frac{\partial T}{\partial t} + \tilde{\mathbf{v}}(x, t) \cdot \nabla T \right) - \nabla \cdot (\mathbf{k} \nabla T) = 0, \quad x \in \Omega \quad (1a)$$

$$-\mathbf{k} \nabla T \cdot \mathbf{n} = q_b(x, t), \quad x \in \Gamma_q \quad (1b)$$

$$T(x, t) = T_b(x, t), \quad x \in \Gamma_T \quad (1c)$$

$$T(x, 0) = T_0(x), \quad x \in \Omega \quad (1d)$$

124 where ρ , c_p , and $\mathbf{k} \in \mathbb{R}^{d \times d}$ are the constant density, heat capacity, and thermal conductivity.
125 Note that our prior work has applied the PIROM to TPS problems with temperature-varying
126 material properties [17]. In the order they appear, the $\rho c_p \frac{\partial T}{\partial t}$ term includes the unsteady
127 energy storage, $\rho c_p \tilde{\mathbf{v}}(x, t) \cdot \nabla T$ includes the temperature advection due to mesh motion, and
128 $\nabla \cdot (\mathbf{k} \nabla T)$ includes the heat conduction. The boundary conditions for the energy equation
129 include Neumann eq. (1b) on Γ_q and Dirichlet eq. (1c) on Γ_T , and the initial condition is
130 provided in eq. (1d).

131 An Arbitrary Lagrangian-Eulerian (ALE) description is used to account for mesh motion
132 due to surface recession. The relative velocity of the material $\tilde{\mathbf{v}}(x, t)$ with respect to the
133 mesh is,

$$\tilde{\mathbf{v}}(x, t) = \mathbf{v}_s(x, t) - \mathbf{v}_m(x, t) \quad (2)$$

134 where $\mathbf{v}_s(x, t)$ and $\mathbf{v}_m(x, t)$ are the physical material velocity and mesh velocity, respectively.
135 In this work, the physical material velocity is assumed to be zero, i.e., $\mathbf{v}_s(x, t) = \mathbf{0}$, and thus
136 the relative velocity is simply the negative of the mesh velocity, $\tilde{\mathbf{v}}(x, t) = -\mathbf{v}_m(x, t)$.

137 2.1.2 Pseudo-Elasticity Equation

138 The mesh motion is described by the steady-state pseudo-elasticity equation without body
139 forces,

$$\nabla \cdot \boldsymbol{\sigma}(\mathbf{w}) = \mathbf{0}, \quad \forall t \in \mathcal{T}, \quad \mathbf{x} \in \Omega \quad (3a)$$

$$\mathbf{w}(\mathbf{x}, t) = \mathbf{w}_q(\mathbf{x}, t), \quad \forall t \in \mathcal{T}, \quad \mathbf{x} \in \Gamma_q \quad (3b)$$

$$\mathbf{w}(\mathbf{x}, t) = \mathbf{0}, \quad \forall t \in \mathcal{T}, \quad \mathbf{x} \in \Gamma_T \quad (3c)$$

$$\mathbf{w}(\mathbf{x}, 0) = \mathbf{0}, \quad \forall \mathbf{x} \in \Omega \quad (3d)$$

140 where the stress tensor $\boldsymbol{\sigma}$ is related to the strain tensor $\boldsymbol{\epsilon}(\mathbf{w})$ through Hooke's law,

$$\boldsymbol{\sigma}(\mathbf{w}) = \mathbb{D} : \boldsymbol{\epsilon}(\mathbf{w})$$

141 where \mathbb{D} is the fourth-order positive definite elasticity tensor, and “ $:$ ” is the double con-
142 traction of the full-order tensor \mathbb{D} with the second-order tensor $\boldsymbol{\epsilon}$. The elasticity tensor
143 ordinarily possess a number of symmetries, effectively reducing the number of components
144 that describe it [2]. The symmetric strain tensor $\boldsymbol{\epsilon}$ measures the deformation of the mesh
145 due to displacements $\mathbf{w}(x, t)$, and is defined as,

$$\boldsymbol{\epsilon}(\mathbf{w}) = \frac{1}{2} (\nabla \mathbf{w} + \nabla \mathbf{w}^\top)$$

¹⁴⁶ The “material” properties for the mesh are chosen to tailor the mesh deformation, and need
¹⁴⁷ not represent the actual material being modeled [1].

¹⁴⁸ For the pseudo-elasticity equations, the boundary conditions include prescribed displacements
¹⁴⁹ $\mathbf{w}_q(x, t)$ on the heated boundary Γ_q in eq. (3b), and zero displacements on the unheated
¹⁵⁰ boundaries in eq. (3c). The initial condition for the mesh displacements is zero in eq. (3d).
¹⁵¹ Particularly, the surface velocity due to the ablating material is a function of the surface
¹⁵² temperature $T_q(x, t)$ for $x \in \Gamma_q$ on the heated boundary. For the i -th material component,
¹⁵³ the mesh velocity on the heated boundary is imposed based on the following relation,

$$\hat{\mathbf{n}} \cdot \mathbf{v}_m(x, t) = f_i(T_q(x, t)), \quad x \in \Gamma_q \quad (4)$$

¹⁵⁴ where $\hat{\mathbf{n}}$ is the unit normal vector on the heated boundary Γ_q , and f_i is a material-dependent
¹⁵⁵ function obtained from tabulated data, commonly referred to as a B’ table [1]. The B’ table
¹⁵⁶ provides a model for the recession velocity as a function of the surface temperature, and is pre-
¹⁵⁷ computed based on high-fidelity simulations or physical experiments for a one-dimensional
¹⁵⁸ slab of materials, and is independent of the TPS geometry. Provided the surface velocity,
¹⁵⁹ the boundary condition in eq. (5) for the mesh displacements are computed by integrating
¹⁶⁰ the surface velocity over time,

$$\mathbf{w}_q(x, t) = \int_0^t \mathbf{v}_m(x, \tau) d\tau \quad (5)$$

¹⁶¹ 2.2 Full-Order Model: Finite-Element Method

¹⁶² The following discussion presents the FOM for predicting the transient thermo-ablative re-
¹⁶³ sponse of the TPS, based on a finite-element discretization of the governing equations in
¹⁶⁴ eq. (1), including the energy equation and pseudo-elasticity equation.

¹⁶⁵ **Energy Equation** To obtain the full-order numerical solution, the *energy equation* is spa-
¹⁶⁶ tially discretized using variational principles of the Discontinuous Galerkin (DG) method [5].
¹⁶⁷ Note that the choice of DG approach is mainly for theoretical convenience, and is exclusively
¹⁶⁸ performed on the energy equation, as it is the surface temperature that drives the ablation
¹⁶⁹ process; the equivalence between DG and FEM is noted upon their convergence. Consider
¹⁷⁰ a conforming mesh partition domain, where each element belongs to one and only one com-
¹⁷¹ ponent. Denote the collection of all M elements as $\{E_i\}_{i=1}^M$. In an element E_i , its shared
¹⁷² boundaries with another element E_j , Neumann BC, and Dirichlet BC are denoted as e_{ij} , e_{iq} ,
¹⁷³ and e_{iT} , respectively. Lastly, $|e|$ denotes the length ($n_d = 2$) or area ($n_d = 3$) of a component
¹⁷⁴ boundary e . For the i -th element, use a set of P trial functions, such as polynomials, to
¹⁷⁵ represent the temperature distribution,

$$T_i(x, t) = \sum_{l=1}^P \phi_l^i(x) u_l^i(t) \equiv \boldsymbol{\phi}_i^\top(x) \mathbf{u}_i(t), \quad i = 1, 2, \dots, M \quad (6)$$

¹⁷⁶ Then, the energy equation is collected into a block-system of ODEs for all the elements in
¹⁷⁷ the mesh,

$$\mathbf{A}\dot{\mathbf{u}} = [\mathbf{B} + \mathbf{C}(\mathbf{u})]\mathbf{u} + \mathbf{f}(t) \quad (7)$$

¹⁷⁸ where $\mathbf{u} = [\mathbf{u}_1, \mathbf{u}_2, \dots, \mathbf{u}_M]^\top \in \mathbb{R}^{MP}$ includes all the DG variables, $\mathbf{f} \in \mathbb{R}^{MP}$ is the external
¹⁷⁹ forcing, and the system matrices \mathbf{A} , \mathbf{B} , and \mathbf{C} are the matrices due to heat capacity, heat
¹⁸⁰ conduction, and temperature advection due to mesh motion, respectively. Note that the
¹⁸¹ advection matrix $\mathbf{C}(\mathbf{u})$ is a function of the temperature \mathbf{u} through the BC in eq. (4), and
¹⁸² corresponds to the main source of non-linearity in the current TPS problem. A detailed
¹⁸³ derivation of eq. (7) and their matrices is provided in Appendix A.

¹⁸⁴ **Pseudo-Elasticity Equation** The *pseudo-elasticity equation* is spatially discretized using
¹⁸⁵ standard FEM [2]. Define the scalar basis functions $\{\psi_q(x)\}_{q=1}^Q$ nodal variables $\{\mathbf{w}_q\}_{q=1}^Q$
¹⁸⁶ for the mesh displacements, where Q is the number of basis functions. Express the mesh
¹⁸⁷ displacements \mathbf{w} at time t as,

$$\mathbf{w}(x, t) \approx \sum_{q=1}^Q \psi_q(x) \mathbf{w}_q \quad (8)$$

¹⁸⁸ Substituting into the Galerkin weak form of the steady pseudo-elasticity equation, the fol-
¹⁸⁹ lowing linear system of equations is obtained for the nodal displacements,

$$\mathbf{K}\mathbf{w} = \mathbf{g} \quad (9)$$

¹⁹⁰ where $\mathbf{K} \in \mathbb{R}^{dQ \times dQ}$ is the global stiffness matrix for the mesh for d dimensions, and \mathbf{g} is the
¹⁹¹ global force vector due to the boundary conditions. The boundary conditions are imposed
¹⁹² by modifying the stiffness matrix \mathbf{K} and the displacement vector \mathbf{w} . The definition of the
¹⁹³ stiffness and forcing vectors follow the standard FEM procedure as detailed in the SIERRA
¹⁹⁴ mechanics module with quadrilateral elements on a structured mesh [2].

¹⁹⁵ 2.3 Reduced-Physics Model

¹⁹⁶ The RPM for predicting the response of the ablating TPS consists of two components: (1) the
¹⁹⁷ *lumped-capacitance model* (LCM), and (2) the *surface recession model* (SRM). The LCM is
¹⁹⁸ described as a first-order system of ODEs for predicting the average temperatures inside the
¹⁹⁹ components of the TPS, and provides a low-fidelity (under estimate) for the component's
²⁰⁰ surface temperature. The SRM provides a relation between the surface temperature and
²⁰¹ the surface recession velocity based on pre-computed B' tables for the material, enabling the
²⁰² computation of one-dimensional surface displacements. The LCM and SRM are combined to
²⁰³ define the RPM, providing low-fidelity estimates for the temperatures and surface recession
²⁰⁴ of the ablating TPS.

²⁰⁵ 2.3.1 Lumped Capacitance Model

²⁰⁶ A general form of the LCM is provided in this section; details regarding the derivation
²⁰⁷ for the four-component TPS used in the results section are provided in Appendix A. The
²⁰⁸ LCM is a classical physics-based low-order model for predicting the temporal variation of

209 average temperature in multiple interconnected components [9]. The LCM is derived at the
210 component level from a point of view of energy conservation, and leads to the following
211 system of ODEs for the average temperatures on the components,

$$\bar{\mathbf{A}}\dot{\bar{\mathbf{u}}} = \bar{\mathbf{B}}\bar{\mathbf{u}} + \bar{\mathbf{f}}(t) \quad (10)$$

212 Where the states and inputs,

$$\bar{\mathbf{u}} = [\bar{u}_1, \bar{u}_2, \dots, \bar{u}_N]^\top \in \mathbb{R}^N, \quad \bar{\mathbf{f}} = [\bar{f}_1, \bar{f}_2, \dots, \bar{f}_N]^\top \in \mathbb{R}^N \quad (11)$$

213 include the average temperatures $\bar{\mathbf{u}}$ and spatially-integrated inputs $\bar{\mathbf{f}}$ for the N components.
214 For $i, j = 1, 2, \dots, N$ the (i, j) -th elements of the $\bar{\mathbf{A}} \in \mathbb{R}^{N \times N}$, $\bar{\mathbf{B}} \in \mathbb{R}^{N \times N}$, and $\bar{\mathbf{f}} \in \mathbb{R}^N$
215 matrices are given by,

$$\bar{A}_i = \begin{cases} \int_{\Omega_i} \rho c_p d\Omega_i, & i = j \\ 0, & i \neq j \end{cases}, \quad \bar{B}_{ij} = \begin{cases} \sum_{j \in \mathcal{N}_i \cup \{T_b\}} \bar{B}_{ij}^i, & i = j \\ \bar{B}_{ij}^{(j)}, & i \neq j \end{cases}, \quad (12a)$$

$$\mathbf{f}_i = \begin{cases} |e_{iq}| \bar{q}_i + \frac{|e_{iT}|}{R_i} \bar{T}_i, & i = j \\ 0, & i \neq j \end{cases} \quad (12b)$$

216 where,

$$\bar{q}_i = \frac{1}{|e_{iq}|} \int_{e_{iq}} q_b d e_{iq}, \quad \bar{T}_i = \frac{1}{|e_{iT}|} \int_{e_{iT}} T_b d e_{iT}, \quad \bar{B}_{ij}^i = -\frac{|e_{ij}|}{R_{ij}}, \quad \bar{B}_{ij}^j = \frac{|e_{ij}|}{R_{ij}} \quad (13)$$

217 where R_{ij} is the equivalent thermal resistance between two neighboring components Ω_i and
218 Ω_j , and R_i is the thermal resistance between component Ω_i and the Dirichlet boundary.
219 The thermal resistances are computed based on the geometry and material properties of the
220 components; details regarding their computation are provided in Appendix A.

221 2.3.2 Surface Recession Model

222 The displacement is assumed to be *one-dimensional* on the heated boundary Γ_q , i.e., the
223 surface recedes only in the direction of the applied load. Displacements perpendicular to
224 the direction of the applied load are assumed small and are neglected. Thus, for the i -th
225 ablating component, the one-dimensional SRM considered in this work takes the form,

$$\dot{\mathbf{w}} = \boldsymbol{\Xi}\bar{\mathbf{u}} - \tilde{\mathbf{f}} \quad (14)$$

226 where $\boldsymbol{\Xi} = \text{diag}(\alpha_1, \dots, \alpha_{\tilde{N}})$ and $\tilde{\mathbf{f}} = (\alpha_1 \bar{u}_{0,1}, \dots, \alpha_{\tilde{N}} \bar{u}_{0,\tilde{N}})^\top$. The constants α_i are small
227 material-dependent constants, determined from the B' table, and $\bar{u}_{0,i}$ is the constant initial
228 temperature of the ablative component. The SRM provides a relation between the surface's
229 temperature and recession velocity, based on pre-computed B' tables for the material.

230 **2.3.3 Thermo-Ablative Reduced-Physics Model**

231 The LCM and SRM are combined to define the RPM for predicting the thermo-ablative
 232 response of the TPS under hypersonic boundary layers. Specifically, the RPM is defined as
 233 the LCM as in eq. (10), where the *geometry- and temperature-dependent matrices* $\bar{\mathbf{A}}$, $\bar{\mathbf{B}}$, and
 234 $\bar{\mathbf{f}}$ are updated at each time step based on the current temperature $\bar{\mathbf{u}}$ and displacements \mathbf{w}
 235 provided by the SRM. The RPM is formally stated as,

$$\tilde{\mathbf{A}}(\mathbf{s})\dot{\mathbf{s}} = \tilde{\mathbf{B}}(\mathbf{s})\mathbf{s} + \tilde{\mathbf{F}}(t) \quad (15a)$$

$$\tilde{\mathbf{z}} = \mathbf{Is} \quad (15b)$$

236 where the state $\mathbf{s} = [\bar{\mathbf{u}}, \mathbf{w}]^\top \in \mathbb{R}^{N+\tilde{N}}$ includes the *average temperature* and *one-dimensional*
 237 *surface displacements*, and \tilde{N} is the number of ablating components with $\tilde{N} \leq N$. Moreover,
 238 the observables are defined as $\mathbf{z} = [\bar{\mathbf{u}}, \mathbf{w}]^\top \in \mathbb{R}^{N+\tilde{N}}$. The matrices are given as,

$$\tilde{\mathbf{A}}(\mathbf{s}) = \begin{bmatrix} \bar{\mathbf{A}}(\mathbf{s}) & \mathbf{0} \\ \mathbf{0} & \mathbf{I} \end{bmatrix}, \quad \tilde{\mathbf{B}}(\mathbf{s}) = \begin{bmatrix} \bar{\mathbf{B}}(\mathbf{s}) & \mathbf{0} \\ \Xi & \mathbf{0} \end{bmatrix}, \quad \tilde{\mathbf{F}}(t) = \begin{bmatrix} \bar{\mathbf{f}}(t) \\ -\mathbf{f} \end{bmatrix} \quad (16)$$

239 In the matrices $\tilde{\mathbf{A}}$ and $\tilde{\mathbf{B}}$, the surface displacements \mathbf{w} are used to define the dimensions for
 240 the Ω_i component used in eqs. (12) and (13), thus effectively coupling the LCM and SRM.

241 **2.4 Summary of Modeling Approaches**

242 The FOM (i.e., FEM) and RPM (i.e., LCM with SRM) are two different but mathematically
 243 connected solution strategies. Particularly, the LCM in eq. (10) not only resembles the
 244 functional form of the DG model in eq. (7), but can be viewed as a special case of the latter,
 245 where the mesh partition is extremely coarse, and the trial and test functions are piece-wise
 246 constants. This removes all spatial variations within each component, and neglects advection
 247 effects due to mesh motion.

248 For example, consider the case where each component Ω_i is treated as one single element,
 249 and each element employs one constant basis function $\phi_i = 1$. The element-wise DG model
 250 in ?? simplifies into a scalar ODE,

$$\mathbf{A}^{(i)} = \bar{A}_i, \quad \mathbf{C}^{(i)} = 0, \quad \mathbf{B}_{ij}^{(i)} = -\sigma|e_{ij}|, \quad \mathbf{B}_{ij}^{(j)} = \sigma|e_{ij}|, \quad \mathbf{f}_i = |e_{iq}|\bar{q}_i + \sigma|e_{iT}|\bar{T}_i \quad (17)$$

251 Clearly, the LCM is a coarse zeroth-order DG model with the inverse of thermal resistance
 252 chosen as the element-wise penalty factors. Or conversely, the DG model is a refined version
 253 of LCM via *hp*-adaptation.

254 The FOM and RPM represent two extremes in the modeling fidelity and computational
 255 cost spectrum. On one hand, the FOM is the most accurate but computationally expensive
 256 to evaluate due to the fine mesh discretizations for both the temperature and displacement
 257 fields, leading to possibly millions of state variables. On the other hand, the RPM consid-
 258 ers only the average temperature of the material, from which the one-dimensional surface
 259 displacements are computed by integrating eq. (14). This considerably reduces the com-
 260 putational cost, but sacrifices local temperature information that are critical to properly
 261 capture higher-order effects due to mesh motion and thermal gradients within each compo-

262 nent. Thus, neither the FOM nor the RPM is an universal approach for real-world analysis,
 263 design, and optimization tasks for ablating TPS, where thousands of high-fidelity model
 264 evaluations may be necessary. This issue motivates the development of the PIROM, which
 265 can achieve the fidelity of FOM at a computational cost close to the RPM, while maintaining
 266 the generalizability to model parameters.

267 3 Physics-Infused Reduced-Order Modeling

268 The formulation of PIROM for ablating TPS starts by connecting the FOM, i.e., the DG-
 269 FEM, and the RPM, i.e., the LCM, via a coarse-graining procedure. This procedure pin-
 270 points the missing dynamics in the LCM when compared to DG-FEM. Subsequently, the
 271 Mori-Zwanzig (MZ) formalism is employed to determine the model form for the missing dy-
 272 namics in PIROM. Lastly, the data-driven identification of the missing dynamics in PIROM
 273 is presented.

274 3.1 Deriving the Reduced-Physics Model via Coarse-Graining

275 The subsequent coarse-graining formulation is performed on the DG-FEM in eq. (7) to
 276 derive the LCM in eq. (10). This process constraints the trial function space of a full-
 277 order DG model to a subset of piece-wise constants, so that the variables \mathbf{u} , matrices \mathbf{A} ,
 278 \mathbf{B} , and \mathbf{C} , and forcing vector \mathbf{f} are all approximated using a single state associated to the
 279 average temperature. Note that the coarse-graining is exclusively performed on the thermal
 280 dynamics, as it is the surface temperature that drives the one-dimensional recession via
 281 the SRM. Hence, the coarse-graining of the mesh dynamics is not included in the following
 282 procedure.

283 3.1.1 Coarse-Graining of States

284 Consider a DG model as in eq. (7) for M elements and an LCM as in eq. (10) for N compo-
 285 nents; clearly $M \gg N$. Let $\mathcal{V}_j = \{i | E_i \in \Omega_j\}$ be the indices of the elements belonging to the
 286 j -th component, so $E_i \in \Omega_j$ for all $i \in \mathcal{V}_j$. The number of elements in the j -th component is
 287 $|\mathcal{V}_j|$. The average temperature on Ω_j is,

$$288 \bar{u}_j = \frac{1}{|\Omega_j|} \sum_{i \in \mathcal{V}_j} \int_{E^{(i)}} \boldsymbol{\phi}^{(i)}(x)^T \mathbf{u}^{(i)} d\Omega = \frac{1}{|\Omega_j|} \sum_{i \in \mathcal{V}_j} |E_i| \boldsymbol{\varphi}_i^{j\top} \mathbf{u}^{(i)}, \quad j = 1, 2, \dots, N \quad (18)$$

288 where $|\Omega_j|$ and $|E_i|$ denote the area ($d = 2$) or volume ($d = 3$) of component j and element
 289 i , respectively. The orthogonal basis functions are defined as $\boldsymbol{\varphi}_i^{j\top} = [1, 0, \dots, 0]^\top \in \mathbb{R}^P$.

290 Conversely, given the average temperatures of the N components, $\bar{\mathbf{u}}$, the states of an
 291 arbitrary element E_i is written as,

$$292 \mathbf{u}^{(i)} = \sum_{k=1}^N \boldsymbol{\varphi}_i^k \bar{u}_k + \delta \mathbf{u}^{(i)}, \quad i = 1, 2, \dots, M \quad (19)$$

292 where $\varphi_i^k = 0$ if $i \notin \mathcal{V}_k$, and $\delta\mathbf{u}^{(i)}$ represents the deviation from the average temperature and
 293 satisfies the orthogonality condition $\varphi_i^{k\top} \delta\mathbf{u}^{(i)} = 0$ for all k .

294 Equations eqs. (18) and (19) are combined and written in matrix form as,

$$\bar{\mathbf{u}} = \Phi^+ \mathbf{u}, \quad \mathbf{u} = \Phi \mathbf{u} + \delta\mathbf{u} \quad (20)$$

295 where $\Phi \in \mathbb{R}^{MP \times N}$ is a matrix of $M \times N$ blocks, with the (i, j) -th block as φ_i^j , $\Phi^+ \in \mathbb{R}^{N \times MP}$
 296 is the left inverse of Φ , with the (i, j) -th block as $\varphi_i^{j+} = \frac{|E_i|}{|\Omega_j|} \varphi_i^{j\top}$, and $\delta\mathbf{u}$ is the collection of
 297 deviations. By their definitions, $\Phi^+ \Phi = \mathbf{I}$ and $\Phi^+ \delta\mathbf{u} = \mathbf{0}$.

298 3.1.2 Coarse-Graining of Dynamics

299 The dependence of the matrices with respect to the displacements \mathbf{w} is dropped to isolate
 300 the analysis based on coarsened variables. Consider a function of states in the form of
 301 $\mathbf{M}(\mathbf{u})\mathbf{g}(\mathbf{u})$, where $\mathbf{g} : \mathbb{R}^{MP} \rightarrow \mathbb{R}^{MP}$ is a vector-valued function, and $\mathbf{M} : \mathbb{R}^{MP} \rightarrow \mathbb{R}^{p \times MP}$
 302 is a matrix-valued function with an arbitrary dimension p . Define the projection matrix
 303 $\mathbf{P} = \Phi \Phi^+$ and the projection operator \mathcal{P} as,

$$\begin{aligned} \mathcal{P}[\mathbf{M}(\mathbf{u})\mathbf{g}(\mathbf{u})] &= \mathbf{M}(\mathbf{P}\mathbf{u})\mathbf{g}(\mathbf{P}\mathbf{u}) \\ &= \mathbf{M}(\Phi\bar{\mathbf{u}})\mathbf{g}(\Phi\bar{\mathbf{u}}) \end{aligned} \quad (21)$$

304 so that the resulting function depends only on the average temperatures $\bar{\mathbf{u}}$. Correspondingly,
 305 the residual operator $\mathcal{Q} = \mathcal{I} - \mathcal{P}$, and $\mathcal{Q}[\mathbf{M}(\mathbf{u})\mathbf{g}(\mathbf{u})] = \mathbf{M}(\mathbf{u})\mathbf{g}(\mathbf{u}) - \mathbf{M}(\Phi\bar{\mathbf{u}})\mathbf{g}(\Phi\bar{\mathbf{u}})$. When
 306 the function is not separable, the projection operator is simply defined as $\mathcal{P}[\mathbf{g}(\mathbf{u})] = \mathbf{g}(\mathbf{P}\mathbf{u})$.

307 Subsequently, the operators defined above are applied to coarse-grain the dynamics. First,
 308 write the DG-FEM in eq. (7) as,

$$\dot{\mathbf{u}} = \mathbf{A}(\mathbf{u})^{-1} \mathbf{B}(\mathbf{u}) \mathbf{u} + \mathbf{A}(\mathbf{u})^{-1} \mathbf{C}(\mathbf{u}) \mathbf{u} + \mathbf{A}(\mathbf{u})^{-1} \mathbf{f}(t) \quad (22)$$

309 and multiply both sides by Φ^+ to obtain,

$$\Phi^+ \dot{\mathbf{u}} = \Phi^+ (\Phi \dot{\bar{\mathbf{u}}} + \delta\dot{\mathbf{u}}) = \dot{\bar{\mathbf{u}}} = \Phi^+ \mathbf{r}(\mathbf{u}, t) \quad (23)$$

310 Apply the projection operator \mathcal{P} and the residual operator \mathcal{Q} to the right-hand side to obtain,

$$\dot{\bar{\mathbf{u}}} = \mathcal{P}[\Phi^+ \mathbf{r}(\mathbf{u}, t)] + \mathcal{Q}[\Phi^+ \mathbf{r}(\mathbf{u}, t)] \equiv \mathbf{r}^{(1)}(\mathbf{u}, t) + \mathbf{r}^{(2)}(\mathbf{u}, t) \quad (24)$$

311 where $\mathbf{r}^{(1)}(\mathbf{u}, t)$ is resolved dynamics that depends on $\bar{\mathbf{u}}$ only, and $\mathbf{r}^{(2)}(\mathbf{u}, t)$ is the un-resolved
 312 or residual dynamics. Detailed derivations and analysis of $\mathbf{r}^{(1)}(\mathbf{u}, t)$ and $\mathbf{r}^{(2)}(\mathbf{u}, t)$ can be
 313 found in the Appendix.

314 It follows from Ref. [17] that the resolved dynamics is exactly the LCM, where the
 315 advection term reduces to zero, i.e., $\bar{\mathbf{C}}(\bar{\mathbf{u}}) = \mathbf{0}$ as shown in the Appendix. Using the notation
 316 from eq. (10), it follows that,

$$\begin{aligned} \mathbf{r}^{(1)}(\mathbf{u}, t) &= \bar{\mathbf{A}}(\bar{\mathbf{u}})^{-1} \bar{\mathbf{B}}(\bar{\mathbf{u}}) \bar{\mathbf{u}} + \bar{\mathbf{A}}(\bar{\mathbf{u}})^{-1} \bar{\mathbf{C}}(\bar{\mathbf{u}}) \bar{\mathbf{u}} + \bar{\mathbf{A}}(\bar{\mathbf{u}})^{-1} \bar{\mathbf{f}}(\bar{\mathbf{u}}) \\ &= \bar{\mathbf{A}}(\bar{\mathbf{u}})^{-1} \bar{\mathbf{B}}(\bar{\mathbf{u}}) \bar{\mathbf{u}} + \bar{\mathbf{A}}(\bar{\mathbf{u}})^{-1} \bar{\mathbf{f}}(t) \end{aligned} \quad (25)$$

317 where the following relations hold,

$$\bar{\mathbf{A}}(\bar{\mathbf{u}}) = \mathbf{W} (\Phi^+ \mathbf{A} (\Phi \bar{\mathbf{u}})^{-1} \Phi)^{-1} \quad \bar{\mathbf{C}}(\bar{\mathbf{u}}) = \mathbf{0} \quad (26a)$$

$$\bar{\mathbf{B}}(\bar{\mathbf{u}}) = \mathbf{W} \Phi^+ \mathbf{B} (\Phi \bar{\mathbf{u}}) \Phi \quad \bar{\mathbf{f}}(t) = \mathbf{W} \Phi^+ \mathbf{f} \quad (26b)$$

318 where $\mathbf{W} \in \mathbb{R}^{N \times N}$ is a diagonal matrix with the i -th element as $[\mathbf{W}]_{ii} = |\mathcal{V}_k|$ if $i \in \mathcal{V}_k$.
 319 The examination of the second residual term $\mathbf{r}^{(2)}(\mathbf{u}, t)$ in eq. (24) is shown in the Appendix,
 320 and demonstrates that the physical sources of missing dynamics in the LCM include: the
 321 approximation of non-uniform temperature within each component as a constant, and the
 322 elimination of the advection term due to coarse-graining. In sum, the above results not
 323 only show that the LCM is a result of coarse-graining of the full-order DG-FEM, but also
 324 reveal the discrepancies between the LCM and the DG-FEM. These discrepancies propagate
 325 into the SRM, which as a result of the averaging in the LCM formulation, under-predicts
 326 the surface recession rates. In the subsequent section, the discrepancies in the LCM are
 327 corrected to formulate the PIROM.

328 3.2 Physics-Infusion Via Mori-Zwanzig Formalism

329 The Mori-Zwanzig (MZ) formalism is an operator-projection technique used to derive ROMs
 330 for high-dimensional dynamical systems, especially in statistical mechanics and fluid dy-
 331 namics [13, 14, 15]. It provides an exact reformulation of a high-dimensional Markovian dy-
 332 namical system, into a low-dimensional observable non-Markovian dynamical system. The
 333 proposed ROM is subsequently developed based on the approximation to the non-Markovian
 334 term in the observable dynamics. Particularly, eq. (24) shows that the DG-FEM dynam-
 335 ics can be decomposed into the resolved dynamics $\mathbf{r}^{(1)}(\mathbf{u}, t)$ and the orthogonal dynamics
 336 $\mathbf{r}^{(2)}(\mathbf{u}, t)$, in the sense of $\mathcal{P}\mathbf{r}^{(2)} = 0$. In this case, the MZ formalism can be invoked to ex-
 337 press the dynamics $\bar{\mathbf{u}}$ in terms of $\bar{\mathbf{u}}$ alone as the projected Generalized Langevin Equation
 338 (GLE) [13, 14, 15],

$$\dot{\bar{\mathbf{u}}}(t) = \mathbf{r}^{(1)}(\bar{\mathbf{u}}, t) + \int_0^t \tilde{\boldsymbol{\kappa}}(t, s, \bar{\mathbf{u}}) ds \quad (27)$$

339 where the first and second terms are referred to as the Markovian and non-Markovian terms,
 340 respectively. The non-Markovian term accounts for the effects of past un-resolved states on
 341 the current resolved states via a memory kernel $\tilde{\boldsymbol{\kappa}}(t, s, \bar{\mathbf{u}})$, which in practice is computa-
 342 tionally expensive to evaluate.

343 3.2.1 Markovian Reformulation

344 This section details the formal derivation of the PIROM as a system of ODEs for the thermal
 345 dynamics, based on approximations to the memory kernel. Specifically, the kernel $\tilde{\mathbf{k}}$ is
 346 examined via a leading-order expansion, based on prior work [19]; this can be viewed as an
 347 analog of zeroth-order holding in linear system theory with a sufficiently small time step. In
 348 this case, the memory kernel is approximated as,

$$\tilde{\boldsymbol{\kappa}}(t, s, \bar{\mathbf{u}}) \approx \mathbf{r}^{(1)}(\bar{\mathbf{u}}, t) \cdot \nabla_{\bar{\mathbf{u}}} \mathbf{r}^{(2)}(\Phi \bar{\mathbf{u}}, t) \quad (28)$$

³⁴⁹ Note that the terms in $\mathbf{r}^{(1)}$ have a common factor $\bar{\mathbf{A}}^{-1}$; this motivates the following heuristic
³⁵⁰ modification of the model form in eq. (27),

$$\dot{\bar{\mathbf{u}}} = \mathbf{r}^{(1)}(\bar{\mathbf{u}}, t) + \bar{\mathbf{A}}^{-1}(\bar{\mathbf{u}}) \int_0^t \boldsymbol{\kappa}(t, s, \bar{\mathbf{u}}) ds \quad (29a)$$

$$\bar{\mathbf{A}}(\bar{\mathbf{u}})\dot{\bar{\mathbf{u}}} = \bar{\mathbf{B}}(\bar{\mathbf{u}})\bar{\mathbf{u}} + \bar{\mathbf{f}}(t) + \int_0^t \boldsymbol{\kappa}(t, s, \bar{\mathbf{u}}) ds \quad (29b)$$

³⁵¹ where the original kernel $\tilde{\boldsymbol{\kappa}}$ is effectively normalized by $\bar{\mathbf{A}}^{-1}$. Intuitively, such choice of kernel
³⁵² reduces its dependency on the averaged material properties, and simplifies the subsequent
³⁵³ design of model form.

³⁵⁴ Subsequently, the hidden states are introduced to “Markovianize” the system eq. (27).
³⁵⁵ In this manner, eq. (29b) is converted into a pure state-space model, with the functional
³⁵⁶ form of the LCM retained; since LCM is a physics-based model, then it encodes the phys-
³⁵⁷ ical information and retains explicit parametric dependence of the problem. Consider the
³⁵⁸ representation of the kernel as a finite sum of simpler functions, e.g., exponentials,

$$\boldsymbol{\kappa}(t, s, \bar{\mathbf{u}}) = \sum_{j=1}^m \mathcal{K}_j(t, s, \bar{\mathbf{u}}) [\mathbf{p}_j + \mathbf{d}_j(\bar{\mathbf{u}})] \phi_j(s, \bar{\mathbf{u}}) \quad (30)$$

³⁵⁹ where,

$$\mathcal{K}_j(t, s, \bar{\mathbf{u}}) = e^{-\int_s^t (\lambda_j + e_j(\bar{\mathbf{u}})) d\tau}, \quad \phi_j(s, \bar{\mathbf{u}}) = \mathbf{q}_j^\top \bar{\mathbf{u}}(s) + \mathbf{g}_j(\bar{\mathbf{u}})^\top \bar{\mathbf{u}}(s) + \mathbf{r}_j^\top \bar{\mathbf{f}}(s) \quad (31)$$

³⁶⁰ with suitable coefficients $\mathbf{p}_j, \mathbf{d}_j, \mathbf{q}_j, \mathbf{g}_j, \mathbf{r}_j \in \mathbb{R}^N$ and decay rates $\lambda_j, e_j(\bar{\mathbf{u}}) > 0$, that need to
³⁶¹ be identified from data.

³⁶² Define the hidden states as,

$$\beta_j(t) = \int_0^t \mathcal{K}_j(s, \bar{\mathbf{u}}) \phi_j(s, \bar{\mathbf{u}}) ds \quad (32)$$

³⁶³ and differentiate with respect to time,,

$$\dot{\beta}_j(t) = -[\lambda_j + e_j(\bar{\mathbf{u}})] \beta_j(t) + \mathbf{q}_j^\top \bar{\mathbf{u}}(t) + \mathbf{g}_j(\bar{\mathbf{u}})^\top \bar{\mathbf{u}}(t) + \mathbf{r}_j^\top \bar{\mathbf{f}}(t) \quad (33)$$

³⁶⁴ to obtain the memory,

$$\int_0^t \boldsymbol{\kappa}(t, s, \bar{\mathbf{u}}) ds = \sum_{j=1}^m [\mathbf{p}_j + \mathbf{d}_j(\bar{\mathbf{u}})] \beta_j(t) \quad (34)$$

³⁶⁵ Then, eq. (29b) is recast as the extended Markovian system,

$$\bar{\mathbf{A}}(\bar{\mathbf{u}})\dot{\bar{\mathbf{u}}} = \bar{\mathbf{B}}(\bar{\mathbf{u}})\bar{\mathbf{u}} + [\mathbf{P} + \mathbf{D}(\bar{\mathbf{u}})] \boldsymbol{\beta} + \bar{\mathbf{f}}(t) \quad (35a)$$

$$\dot{\boldsymbol{\beta}} = [\mathbf{Q} + \mathbf{G}(\bar{\mathbf{u}})] \bar{\mathbf{u}} + [\mathbf{E}(\bar{\mathbf{u}}) - \boldsymbol{\Lambda}] \boldsymbol{\beta} + \mathbf{R}\bar{\mathbf{f}}(t) \quad (35b)$$

366 where the data-driven operators associated to the hidden dynamics are collected as,

$$\Lambda = \text{diag}(\lambda_1, \lambda_2, \dots, \lambda_m) \in \mathbb{R}^{m \times m}, \quad \mathbf{P} = [\mathbf{p}_1, \mathbf{p}_2, \dots, \mathbf{p}_m] \in \mathbb{R}^{N \times m} \quad (36a)$$

$$\mathbf{D}(\bar{\mathbf{u}}) = [\mathbf{d}_1(\bar{\mathbf{u}}), \mathbf{d}_2(\bar{\mathbf{u}}), \dots, \mathbf{d}_m(\bar{\mathbf{u}})] \in \mathbb{R}^{N \times m}, \quad \mathbf{Q} = [\mathbf{q}_1, \mathbf{q}_2, \dots, \mathbf{q}_m] \in \mathbb{R}^{m \times N} \quad (36b)$$

$$\mathbf{G}(\bar{\mathbf{u}}) = [\mathbf{g}_1(\bar{\mathbf{u}}), \mathbf{g}_2(\bar{\mathbf{u}}), \dots, \mathbf{g}_m(\bar{\mathbf{u}})] \in \mathbb{R}^{m \times N}, \quad \mathbf{R} = [\mathbf{r}_1, \mathbf{r}_2, \dots, \mathbf{r}_m] \in \mathbb{R}^{m \times N} \quad (36c)$$

$$\mathbf{E}(\bar{\mathbf{u}}) = \text{diag}(e_1(\bar{\mathbf{u}}), e_2(\bar{\mathbf{u}}), \dots, e_m(\bar{\mathbf{u}})) \in \mathbb{R}^{m \times m} \quad (36d)$$

367 The form of the temperature-dependent matrices $\mathbf{D}(\bar{\mathbf{u}})$, $\mathbf{G}(\bar{\mathbf{u}})$, and $\mathbf{E}(\bar{\mathbf{u}})$ is specified in the
368 next section. Since the hidden states β serve as the memory, their initial conditions are set
369 to zero, i.e., $\beta(t_0) = \mathbf{0}$, no memory at the beginning. The physics-infused model in eq. (35)
370 retains the structure of the LCM, while the hidden states account for missing physics through
371 corrections to the stiffness and advection matrices, as well as the forcing term.

372 3.2.2 Coupled Physics-Infused Model

373 The next step involves coupling the physics-infused model in eq. (35) with the SRM in
374 eq. (14) to define the PIROM for ablating TPS. To this end, define the observables as the
375 surface temperature $\mathbf{z}_u \in \mathbb{R}^{\tilde{N}}$ and displacements $\mathbf{z}_w \in \mathbb{R}^{\tilde{N}}$ for $\tilde{N} \leq N$ ablating components
376 to define the observable vector as $\mathbf{z} = [\mathbf{z}_u, \mathbf{z}_w]^\top \in \mathbb{R}^{n_z}$ with $n_z = 2\tilde{N}$ as the total number of
377 observables.

378 Collect the RPM and hidden states into a single state vector $\mathbf{y} = [\bar{\mathbf{u}}, \mathbf{w}, \beta]^\top \in \mathbb{R}^{n_y}$, where
379 $n_y = N + \tilde{N} + m$, and define a data-driven operator $\mathbf{M} \in \mathbb{R}^{n_z \times n_y}$ to define the PIROM's
380 observable as,

$$\mathbf{z} = \mathbf{My} \quad (37)$$

381 where,

$$\mathbf{M} = \begin{bmatrix} \mathbf{M}_{\bar{u}} & \mathbf{0} & \mathbf{M}_\beta \\ \mathbf{0} & \mathbf{I} & \mathbf{0} \end{bmatrix} \quad (38)$$

382 includes the matrices $\mathbf{M}_{\bar{u}} \in \mathbb{R}^{\tilde{N} \times N}$ and $\mathbf{M}_\beta \in \mathbb{R}^{\tilde{N} \times m}$, which computes the surface tempera-
383 ture observable from the RPM states and hidden states, respectively. The PIROM is coupled
384 to the SRM in eq. (14) by leveraging eq. (37) to compute the surface recession velocity. Thus,
385 the PIROM is formally stated as,

$$\mathcal{A}\dot{\mathbf{y}} = [\mathcal{B} + \mathcal{C}]\mathbf{y} + \mathcal{F}(t) \quad (39a)$$

$$\mathbf{z} = \mathbf{My} \quad (39b)$$

386 where,

$$\mathcal{A} = \begin{bmatrix} \bar{\mathbf{A}} & \mathbf{O} & \mathbf{O} \\ \mathbf{O} & \mathbf{I} & \mathbf{O} \\ \mathbf{O} & \mathbf{O} & \mathbf{I} \end{bmatrix} \in \mathbb{R}^{n_y \times n_y}, \quad \mathcal{B} = \begin{bmatrix} \bar{\mathbf{B}} & \mathbf{O} & \mathbf{P} \\ \Xi\mathbf{M}_u & \mathbf{O} & \Xi\mathbf{M}_\beta \\ \mathbf{Q} & \mathbf{O} & -\Lambda \end{bmatrix} \in \mathbb{R}^{n_y \times n_y}, \quad (40a)$$

$$\mathcal{C} = \begin{bmatrix} \mathbf{O} & \mathbf{O} & \mathbf{D}(\bar{\mathbf{u}}) \\ \mathbf{O} & \mathbf{O} & \mathbf{O} \\ \mathbf{G}(\bar{\mathbf{u}}) & \mathbf{O} & \mathbf{E}(\bar{\mathbf{u}}) \end{bmatrix} \in \mathbb{R}^{n_y \times n_y}, \quad \mathcal{F} = \begin{bmatrix} \bar{\mathbf{f}}(t) \\ -\bar{\mathbf{f}} \\ \mathbf{R}\bar{\mathbf{f}}(t) \end{bmatrix} \in \mathbb{R}^{n_y} \quad (40b)$$

387 The learnable parameters in the PIROM are collected as,

$$\Theta = \{\mathbf{P}, \mathbf{Q}, \mathbf{R}, \mathbf{D}(\bar{\mathbf{u}}), \mathbf{G}(\bar{\mathbf{u}}), \mathbf{E}(\bar{\mathbf{u}}), \mathbf{M}_u, \mathbf{M}_\beta\}, \in \mathbb{R}^{n_\theta} \quad (41)$$

388 Particularly, the matrices $\mathbf{P}, \mathbf{\Lambda}, \mathbf{Q}, \mathbf{R}$ are constants that need to be identified from data, and
 389 account for the effects of coarse-graining on the stiffness and forcing matrices. The matrices
 390 $\mathbf{D}(\bar{\mathbf{u}}), \mathbf{E}(\bar{\mathbf{u}}), \mathbf{G}(\bar{\mathbf{u}})$ are state-dependent matrices, and account for the effects of coarse-graining
 391 on the advection matrix due to mesh motion. Leveraging the DG-FEM formula for the
 392 advection matrix in eq. (56c) in the Appendix, and noting that the ablating velocity in
 393 eq. (4) imposes the boundary condition for the mesh motion, the state-dependent matrices
 394 for the i -th component are written as,

$$\mathbf{D}(\bar{\mathbf{u}}) \approx \dot{\mathbf{w}}(\bar{\mathbf{u}}) \odot_r \mathbf{D}, \quad \mathbf{G}(\bar{\mathbf{u}}) \approx \mathbf{G} \odot_r \dot{\mathbf{w}}(\bar{\mathbf{u}}), \quad \mathbf{E}(\bar{\mathbf{u}}) \approx \dot{\mathbf{W}}(\bar{\mathbf{u}}) \odot \mathbf{E} \quad (42)$$

395 where $\dot{\mathbf{w}}(\bar{\mathbf{u}})$ is the SRM based on the observable temperature $\bar{\mathbf{u}}$, \odot_r is the row-wise multiplication,
 396 and $\dot{\mathbf{W}}$ is the concatenation of $\dot{\mathbf{w}}$ for \tilde{m} times, where \tilde{m} corresponds to the number
 397 of hidden states per component, i.e., $m = N\tilde{m}$.

398 The PIROM in eq. (39) incorporates explicit information on the material properties,
 399 boundary conditions, and surface recession, and is designed to generalize across parametric
 400 variations in these inputs. Moreover, the hidden dynamics in eq. (35) are interpretable, as
 401 these retain the functional form of the DG-FEM in eq. (7). The next step is focused on
 402 identifying the unknown data-driven parameters Θ characterizing the hidden dynamics.

403 3.3 Learning the Hidden Dynamics

404 Learning of the PIROM is achieved through a gradient-based neural-ODE-like approach [3].
 405 For ease of presentation, consider the compact form of the PIROM in eq. (39),

$$\mathcal{D}(\dot{\mathbf{y}}, \mathbf{y}, \boldsymbol{\xi}, \mathcal{F}; \Theta) = \mathbf{0} \quad (43)$$

406 where $\boldsymbol{\xi}$ defines the model parameters, i.e., material properties and B' tables, while \mathcal{F}
 407 represents the forcing terms, i.e., the boundary conditions.

408 Consider a dataset of N_s high-fidelity *surface temperature* observable trajectories \mathbf{z}_{HF} ,
 409 sampled at p time instances $\{t_k\}_{k=0}^{p-1}$, for different parameter settings $\{\boldsymbol{\xi}^{(l)}\}_{l=1}^{N_s}$ and forcing
 410 functions $\{\mathcal{F}^{(l)}(t)\}_{l=1}^{N_s}$. The dataset is expressed as,

$$\mathcal{D} = \left\{ \left(t_k, \mathbf{z}_{HF}^{(l)}(t_k), \boldsymbol{\xi}^{(l)}, \mathcal{F}^{(l)}(t_k) \right) \right\}_{l=1}^{N_s}, \quad k = 0, 1, \dots, p-1 \quad (44)$$

411 In this work, the dataset contains only surface temperature observables – all high-fidelity
 412 information regarding the surface displacements *are assumed to be unavailable during learning*.
 413

414 The learning problem is formulated as the following differentially-constrained problem,

$$\min_{\Theta} \quad \mathcal{J}(\Theta; \mathcal{D}) = \sum_{l=1}^{N_s} \int_{t_0}^{t_f} \ell \left(\mathbf{z}_u^{(l)}, \mathbf{z}_{HF}^{(l)} \right) dt \quad (45a)$$

$$\text{s.t.} \quad \mathbf{0} = \mathcal{D} \left(\dot{\mathbf{y}}^{(l)}, \mathbf{y}^{(l)}, \boldsymbol{\xi}^{(l)}, \mathcal{F}^{(l)}; \Theta \right) \quad (45b)$$

415 for $l = 1, 2, \dots, N_s$, the objective is to minimize the discrepancy between the high-fidelity
 416 and PIROM predictions for the l -th trajectory with $\ell \left(\mathbf{z}_u^{(l)}, \mathbf{z}_{HF}^{(l)} \right) = \left\| \mathbf{z}_u^{(l)} - \mathbf{z}_{HF}^{(l)} \right\|_2^2$.

417 The gradient-based optimization loop is based on the adjoint variable $\boldsymbol{\lambda}$, governed by the
 418 adjoint differential equation,

$$\frac{\partial \ell}{\partial \mathbf{y}} + \boldsymbol{\lambda}^\top \frac{\partial \mathcal{D}}{\partial \mathbf{y}} - \frac{d}{dt} \left(\boldsymbol{\lambda}^\top \frac{\partial \mathcal{D}}{\partial \dot{\mathbf{y}}} \right) = \mathbf{0} \quad (46a)$$

$$\boldsymbol{\lambda}(t_f)^\top \frac{\partial \mathcal{D}}{\partial \dot{\mathbf{y}}(t_f)} = \mathbf{0} \quad (46b)$$

419 Once $\boldsymbol{\lambda}$ is solved, the gradient is computed as,

$$\nabla_\Theta \mathcal{J} = \frac{1}{N_s} \sum_{l=1}^{N_s} \int_{t_0}^{t_f} \left(\frac{\partial \ell}{\partial \Theta} + (\boldsymbol{\lambda}^{(l)})^\top \frac{\partial \mathcal{D}}{\partial \Theta} \right) dt \quad (47)$$

420 4 Application to Thermal Protection Systems

421 In this section, the proposed PIROM approach is applied to the analysis of thermo-ablative
 422 multi-layered hypersonic TPS. The performance of the PIROM is evaluated in terms of the
 423 three corners of the ITM in Fig. 1, across a wide range of boundary condition and SRM
 424 model parametrizations for the TPS. The results show PIROM to be a promising candidate
 425 for the solution of the impossible trinity of modeling, achieving RPM-level computational
 426 efficiency and generalizability, while attaining high-fidelity model accuracy.

427 4.1 Problem Definition

428 Consider the two-dimensional TPS configuration shown in Fig. 3 with constant material
 429 properties within each layer, dimensions, and BCs listed in Table 1. Such configuration is
 430 representative of the TPS used for the initial concept 3.X vehicle in past studies [10], and in-
 431 volves two main layers: an outer ablative layer, and an inner substrate layer. The top ablative
 432 layer may be composed of different materials, such as PICA or Avcoat, while the substrate
 433 layer is typically made of a high-temperature resistant material, such as carbon-carbon com-
 434 posite [7]. The ablative layer, composed of $\tilde{N} = 3$ ablative components, is subjected to
 435 strong time-varying and non-uniform heating, while the substrate layer, composed of one
 436 non-ablative component, is insulated adiabatically at the outer surface; the total number of
 437 components is thus $N = 4$.

438 The lumped-mass representation of the TPS configuration is shown in Fig. 3(b), where

Component	w (cm)	h (cm)	ρ (kg/m ³)	c_p (J/kg·K)	k (W/m·K)	$\alpha \times 10^{-6}$ (m/s·K)
#1	0.3	0.03	160	1200	0.2	1
#2	0.3	0.03	1800	900	5	1
#3	0.3	0.03	300	1500	0.15	1
#4	0.9	0.03	1600	800	10	0

Table 1: Description of TPS components, including thickness h , density ρ , specific heat capacity c_p , thermal conductivity k , and SRM parameter α .

each component Ω_i is represented by a lumped mass with uniform temperature $u_i(t)$. Details regarding the derivation of the LCM for this configuration are provided in Appendix A. The sources of non-linearities studied in this problem originate from the coupling between the thermodynamics and temperature-dependent mesh motion, i.e., geometry-dependent matrices, as well as the heterogeneities across material layers. As shown in Fig. 3, perfect thermocouple devices are placed at the surfaces of the ablative layers for the collection of the high-fidelity temperature signals that are used in the following sections for training and testing the PIROM.

4.2 Problem Parametrization

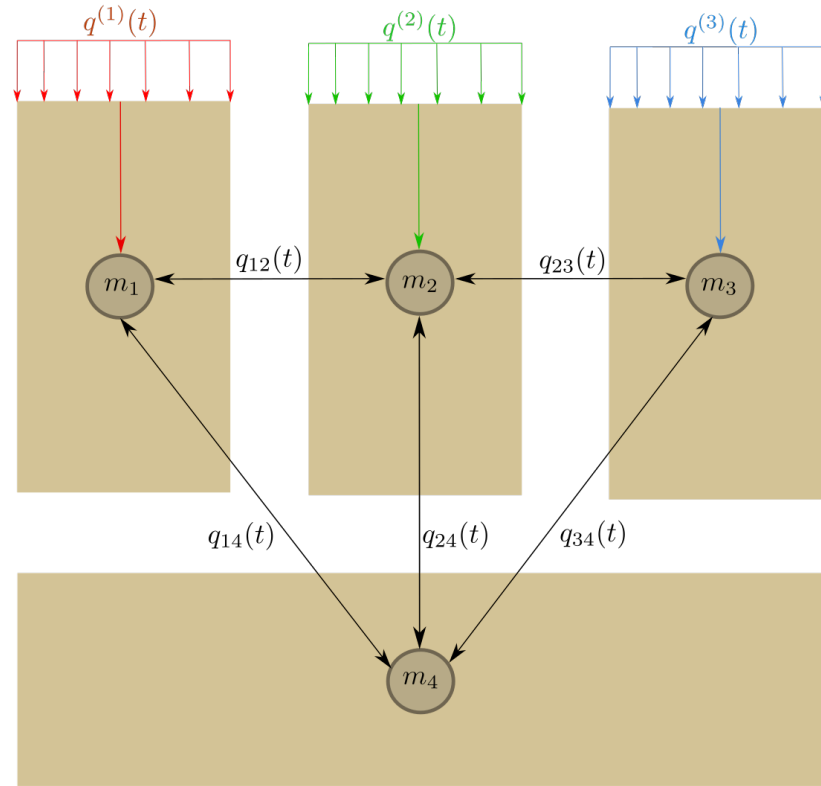
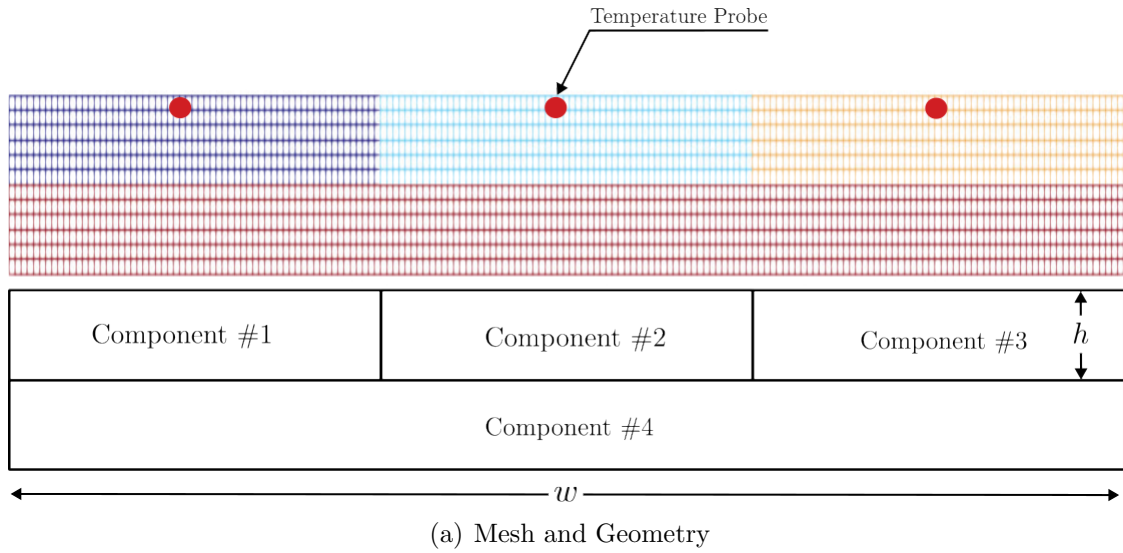
The operating conditions of the TPS are specified by the boundary conditions, i.e., the heat flux, and the surface recession model (SRM). Specifically, the heat flux on the Neumann BC is parametrized using $\xi_{\text{BC}} = \{\xi_0, \xi_1, \xi_2\}$, while the SRM is parametrized using $\xi_{\text{SRM}} = \{\alpha_1, \alpha_2, \alpha_3\}$. Thus, the heat flux and SRM over the i -th ablative component are expressed as,

$$q_i(x, t; \xi_{\text{BC}}) = \xi_0 e^{\xi_1 x} e^{\xi_2 t}, \quad \forall x \in \Gamma_{i,q}, \quad \dot{w}_i(z_{u,i}; \xi_{\text{SRM}}) = \alpha_i (z_{u,i} - u_{0,i}), \quad i = 1, \dots, \tilde{N} \quad (48)$$

where $\Gamma_{i,q}$, $z_{u,i}$, and $u_{0,i}$ correspond to the Neumann BC surface, the PIROM's surface temperature prediction, and the initial temperature of the i -th ablative component, respectively. The parameters ξ_0 , ξ_1 , and ξ_2 control the heat flux magnitude, spatial variation, and temporal variation, respectively. The constant α_i is a small material-dependent constant determined from the B' table [12], specifying the surface recession velocity for a given temperature.

4.3 Data Generation

Full-order solutions of the TPS are computed using the FEM multi-mechanics module from the **Aria** package [4], where the mesh is shown in Fig. 3. The mesh consists of 2196 total elements, with 366 elements for each ablative component and 1098 elements for the substrate component. Given an operating condition $\xi = [\xi_{\text{BC}}, \xi_{\text{SRM}}]^\top$, a high-fidelity solution is computed for one minute, starting from an uniform initial temperature of $T(x, t_0) = 300$ K. Each solution consist of a collection of space-time-varying temperature and displacement fields $\left\{ \left(t_k, \mathbf{u}_{\text{HF}}^{(l)}(t_k), \mathbf{w}_{\text{HF}}^{(l)}(t_k), \xi^{(l)} \right) \right\}_{k=0}^{p-1}$, where p is the number of time steps with a step size of $\Delta t \approx 10^{-3}$. The observable trajectories are representative of near-wall thermocouple sens-



(b) Lumped Mass Representation

Figure 3: Four-component TPS geometry and lumped-mass representation for the TPS.

ing of hypersonic flows involving heat transfer. At each time instance t_k , a temperature reading is recorded from each ablative component using the thermocouples shown in Fig. 3, resulting in three temperature signals, i.e., the observables $\mathbf{z}_{\text{HF}} \in \mathbb{R}^3$. Therefore, each full-order solution produces one trajectory of observables $\left\{ \left(t_k, \mathbf{z}_{\text{HF}}^{(l)}(t_k), \boldsymbol{\xi}^{(l)} \right) \right\}_{k=0}^{p-1}$. The goal of the PIROM is to predict the surface temperature and displacement as accurately as possible.

4.3.1 Definition of Training and Testing Datasets

The range of parameters used to generate the training \mathcal{D}_1 and testing $\{\mathcal{D}_2, \mathcal{D}_3\}$ datasets are listed in Table 1. The training and testing datasets are designed, respectively, to: (1) minimize the information that the PIROM can “see”, and (2) to maximize the variability of test operating conditions to examine the PIROM’s generalization performance. A total of 110 normally-distributed data points for the BC parametrization are visualized in Fig. 4(a), and the corresponding observable trajectories are shown in Figs. 4(b) and 4(c). The training dataset \mathcal{D}_1 includes 10 trajectories with randomly selected BC parameters from the 110 points, with nominal SRM parameters $\boldsymbol{\xi}_{\text{SRM}} = \{1, 1, 1\} \times 10^{-6}$. Note that although Fig. 4(c) shows the surface displacements for all ablative components in \mathcal{D}_1 , only the *surface temperature is used for training the PIROM*.

Two additional datasets are generated for testing. The dataset \mathcal{D}_2 includes the remaining 100 BC parameter values not considered in \mathcal{D}_1 , and the high-fidelity simulation are generated with the same nominal SRM parameters. The cases in the \mathcal{D}_3 fixes the boundary condition as shown in Fig. 4(a) and varies the SRM parameters as shown in Table. 1. The testing datasets \mathcal{D}_2 and \mathcal{D}_3 are *out-of-distribution* (OOD) datasets, and are meant for testing the generalizability of the ROMs to unseen BCs and SRMs, respectively.

4.4 Performance Metrics

The performance of the PIROM is evaluated by the metrics of prediction error and computational cost.

Prediction Error Consider one trajectory of high-fidelity surface temperature and displacement data $\left\{ \left(t_k, \mathbf{z}_{u,\text{HF}}^{(l)}(t_k), \mathbf{z}_{w,\text{HF}}^{(l)}(t_k) \right) \right\}_{k=0}^{p-1}$ for the l -th operating condition in the testing datasets \mathcal{D}_2 or \mathcal{D}_3 . The difference $e_i^{(l)}$ for the i -th predicted observable, denoted as $z_i^{(l)}$, is computed as,

$$e_i^{(l)} = \frac{1}{\Delta z_i^{(l)}} \sqrt{\frac{1}{p} \sum_{k=0}^{p-1} \left(z_{i,\text{HF}}^{(l)}(t_k) - z_i^{(l)}(t_k) \right)^2} \quad (49)$$

for $i = 1, 2, 3$ and $z_i^{(l)} \in \{z_{i,u}^{(l)}, z_{i,w}^{(l)}\}$, and where,

$$\Delta z_i^{(l)} = \max_{0 \leq k \leq p-1} z_{i,\text{HF}}^{(l)}(t_k) - \min_{0 \leq k \leq p-1} z_{i,\text{HF}}^{(l)}(t_k) \quad (50)$$

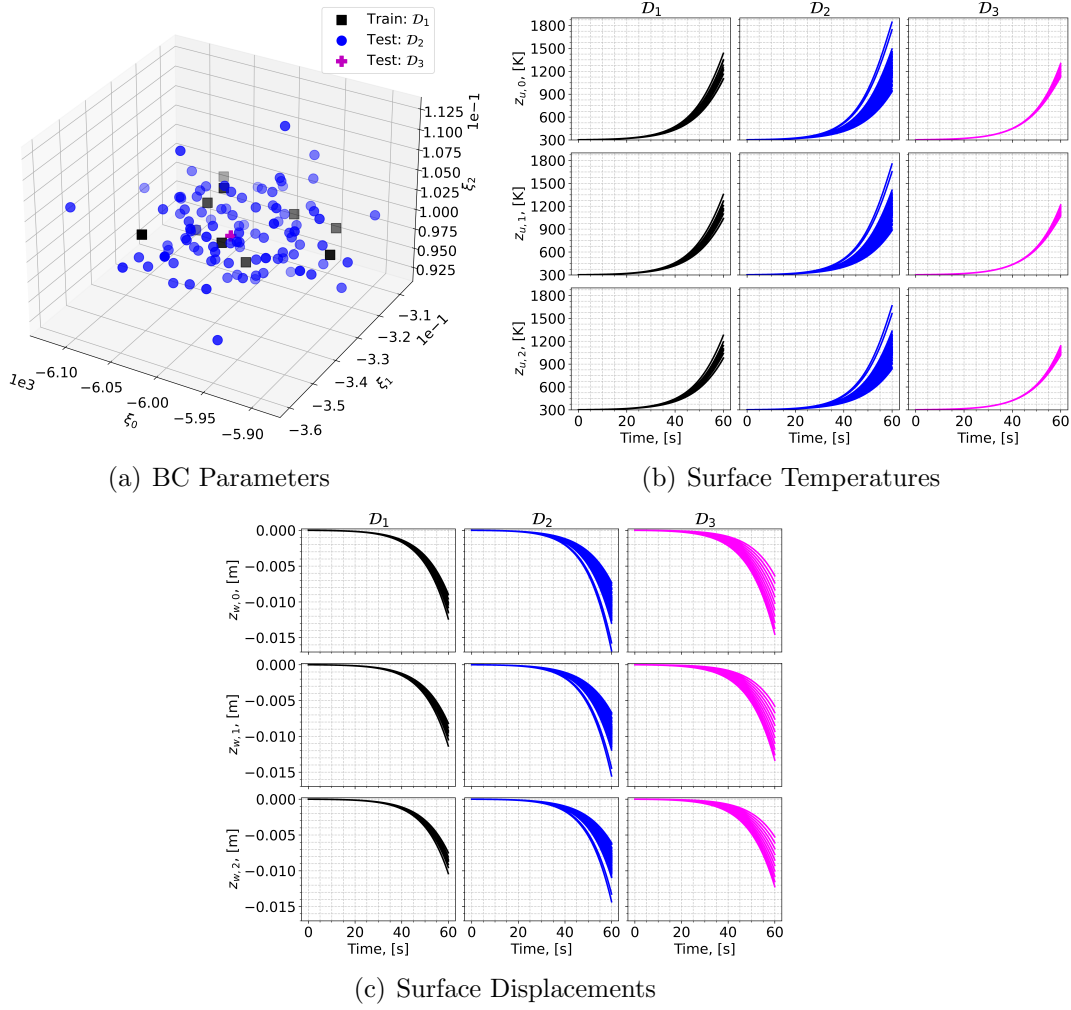


Figure 4: Boundary condition parameters, temperature observables, and displacement observables for the training and testing datasets. The variables $z_{u,i}$ and $z_{w,i}$ correspond to the surface temperature and displacement of the i -th ablative component, respectively.

⁴⁹⁷ Subsequently, the prediction error of one trajectory is computed by a weighted sum based
⁴⁹⁸ on the area of each *ablative component*, resulting in the normalized root mean square error
⁴⁹⁹ (NRMSE) metric for one trajectory,

$$\text{NRMSE} = \frac{\sum_{i=1}^{\tilde{N}} |\Omega_i| e_i^{(l)}}{\sum_{i=1}^{\tilde{N}} |\Omega_i|} \times 100\% \quad (51)$$

⁵⁰⁰ For one dataset, the NRMSE is defined to be the average of the NRMSEs of all trajectories
⁵⁰¹ in the dataset.

⁵⁰² **Computational Acceleration** The *computational acceleration* metric focuses on the quan-
⁵⁰³ tification of the speedup factor $\frac{\mathcal{T}_{\text{HF}}(\mathcal{D})}{\mathcal{T}_{\mathcal{M}}(\mathcal{D})}$, where $\mathcal{T}_{\text{HF}}(\mathcal{D})$ and $\mathcal{T}_{\mathcal{M}}(\mathcal{D})$ correspond to the wall-clock
⁵⁰⁴ time required by the high-fidelity model and the reduced-order model \mathcal{M} (i.e., PIROM or
⁵⁰⁵ RPM) to evaluate all trajectories in the dataset \mathcal{D} , respectively. For a benchmark analysis
⁵⁰⁶ of the computational costs during the training phase, please refer to Ref. [17].

⁵⁰⁷ 4.5 Generalization to Boundary Conditions

⁵⁰⁸ To assess generalization to BC, the PIROM and RPM are evaluated on the \mathcal{D}_2 dataset. Tem-
⁵⁰⁹ perature trajectory predictions for a representative test case are shown in Figs. 5(a) and 5(b),
⁵¹⁰ where the PIROM accurately captures the surface temperature and displacement dynamics,
⁵¹¹ while the RPM exhibits larger deviations and under-predicts surface displacements due to
⁵¹² the averaging effects of the LCM. The mean NRMSE across all test cases in \mathcal{D}_2 is shown
⁵¹³ in Figs. 5(e) and 5(f), where the PIROM consistently achieves errors of $\approx 0.5\%$ for both
⁵¹⁴ temperature and displacement predictions, improving the RPM's accuracy by an order of
⁵¹⁵ magnitude. Figure 5 reports the average substrate temperature, where the LCM remains
⁵¹⁶ highly accurate due to the symmetric TPS geometry, adiabatic BCs, and negligible thermal
⁵¹⁷ gradients within the substrate. Although the PIROM is trained only on the surface tem-
⁵¹⁸ peratures of the three ablative components, its hidden dynamics retain the LCM's accuracy
⁵¹⁹ for this untrained observable, demonstrating the PIROM's ability to generalize and preserve
⁵²⁰ the underlying physics of the reduced-physics backbone.

⁵²¹ 4.6 Generalization to Surface Recession Models

⁵²² The generalization performance of the PIROM and RPM is also evaluated on surface reces-
⁵²³ sion models using the \mathcal{D}_3 dataset. As detailed in Table 1, the SRM parameter α in \mathcal{D}_3 is
⁵²⁴ perturbed 10 times by up to $\pm 50\%$ from their nominal values. The SRM model perturbation
⁵²⁵ introduces significant changes to the ablative layer dynamics, potentially increasing the rate
⁵²⁶ of ablation at lower temperatures, as shown in Figs. 5(c) and 5(d). The PIROM, without
⁵²⁷ considering any SRM variations during training, is able to accurately predict the surface tem-
⁵²⁸ perature and displacement dynamics for the perturbed SRMs. Figures 5(e) and 5(f) show
⁵²⁹ the mean NRMSE across all test cases in \mathcal{D}_3 , where the PIROM consistently achieves errors
⁵³⁰ below 1.5% for both temperature and displacement predictions, and consistently improves
⁵³¹ the RPM's accuracy by approximately an order of magnitude.

532 **4.7 Computational Cost**

533 All computations are performed in serial for fairness on an Intel Xeon (R) Gold 6258R
534 CPU 2.70GHz computer with 62 GB of RAM. The numerical integration for the RPM
535 and PIROM models are performed using SciPy's `solve_ivp` function with default settings.
536 Provided a parametrization for the BC and SRM, the high-fidelity FEM simulation takes
537 about ≈ 60 seconds, the RPM takes about ≈ 0.137 seconds, and the PIROM takes about
538 ≈ 0.280 seconds. Therefore, during evaluation both the RPM and PIROM achieve speedup
539 factors of approximately 438 and 214, respectively, over the high-fidelity model. As a result,
540 the PIROM and RPM are *two-orders-of-magnitude faster* than the high-fidelity model. The
541 PIROM nearly preserves the computational efficiency of the RPM (about twice as expensive
542 as the RPM), while achieving significantly higher accuracy and generalization capabilities.
543 The results demonstrate the benefits of physics-infused modeling for the development of
544 efficient and generalizable ROMs for complex multi-physics systems.

545 **4.8 Summary of Results**

546 The results presented in this section demonstrate the accuracy, generalizability, and com-
547 putational efficiency of the proposed PIROM approach for the analysis of thermo-ablative
548 multi-layered hypersonic TPS. The PIROM consistently achieves low prediction errors below
549 1% for both surface temperature and displacement across a range of unseen boundary con-
550 ditions and surface recession models. Furthermore, the PIROM retains the computational
551 efficiency of traditional RPMs, achieving speedup factors of over 200 times compared to high-
552 fidelity FEM simulations. The generalization capabilities of the PIROM are attributed to its
553 hybrid structure: a physics-based LCM backbone that ensures consistency with the under-
554 lying thermodynamics, while a data-driven correction mechanism captures the un-resolved
555 dynamics.

556 **5 Conclusions**

557 This work presents the development and validation of the *scientific machine learning* frame-
558 work termed *Physics-Informed Reduced Order Model* (PIROM) for simulating the transient
559 thermo-ablative response of hypersonic thermal protection systems (TPS) subjected to hy-
560 personic aerodynamic heating. Using coarse-graining on a DG-FEM model and the Mori-
561 Zwanzig formalism, the PIROM formulation in Ref. [17] is extended to account for non-
562 decomposing ablative material response. The PIROM builds upon the following two key
563 components: (1) a first-order physics-based model, i.e., the LCM and SRM, for low-fidelity
564 predictions of the transient thermo-ablative TPS response; and (2) a data-driven closure to
565 the non-Markovian term in the generalized Langevin equation (GLE). The non-Markovian
566 closure is recast as a set of hidden states that evolve according to a data-driven dynamical
567 system that is learned from a sparse collection of high-fidelity temperature signals.

568 The results demonstrate that the PIROM framework effectively reconciles the trade-
569 offs between accuracy, generalizability, and efficiency of the ITM for simulating ablating
570 hypersonic TPS. The PIROM consistently achieves mean observable prediction errors of

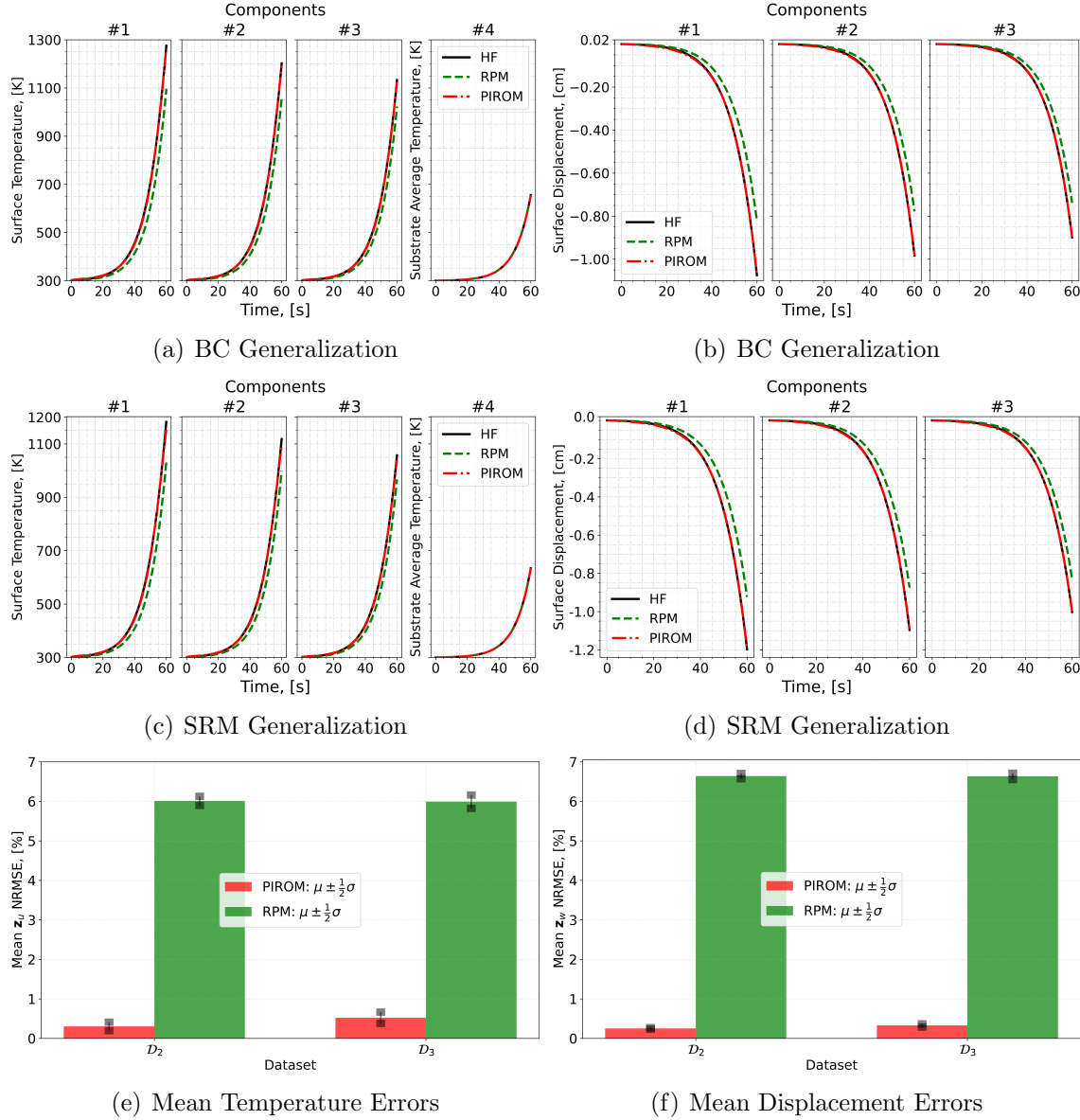


Figure 5: PIROM predictions against high-fidelity solutions for (a)-(b) BC generalization, (c)-(d) SRM generalization, and (e)-(f) mean errors across testing datasets.

571 $\approx 0.5\%$ for a wide range of extrapolative settings of model parameters, involving time-and-
572 space varying boundary conditions and SRM models. Notably, the PIROM improves the
573 RPM’s accuracy by an order of magnitude while preserving its computational efficiency,
574 physical interpretability, and parametric generalizability. Moreover, the PIROM delivers
575 online evaluations that are two orders of magnitude faster than the FOM. These results
576 highlight the PIROM’s potential as a promising framework for optimizing multi-physical
577 dynamical systems, such as TPS under diverse operating conditions.

578 A Technical Details

579 This appendix presents the technical details of the PIROM framework applied to the trans-
 580ient modeling of thermo-ablative TPS. The first section provides the mathematical details
 581 for the definition of the DG-FEM. The second section details the coarse-graining proce-
 582 dures performed on the DG-FEM representation of the TPS. The third section presents the
 583 derivation of the LCM model from an energy-conservation perspective.

584 A.1 Full-Order Model

585 To obtain the full-order numerical solution, the governing equation is spatially discretized
 586 using variational principles of Discontinuous Galerkin (DG) to result in a high-dimensional
 587 system of ordinary differential equations (ODEs). The DG-FEM model is written in an
 588 element-wise form, which is beneficial for subsequent derivations of the lower-order models.
 589 Note that the choice of DG approach here is mainly for theoretical convenience in the sub-
 590 sequent coarse-graining formulation. In the numerical results, the full-order TPS ablation
 591 simulations is computed using standard FEM instead, and the equivalence between DG and
 592 standard FEM is noted upon their convergence.

593 A.1.1 Domain Discretization

594 Consider a conforming mesh partition of the domain in Fig. 3, where each element belongs
 595 to one and only one component. Denote the collection of all M elements as $\{E_i\}_{i=1}^M$. To ease
 596 the description of the DG model, a graph structure is employed. The elements are treated
 597 as vertices, the set of which is denoted $\mathcal{V} = \{m\}_{m=1}^M$. Two neighboring elements, E_i and E_j ,
 598 are connected by an edge (i, j) , and the shared boundary between them is denoted e_{ij} . The
 599 collection of all edges are denoted \mathcal{E} , and \mathcal{G} is referred to as a graph. In the graph, the edges
 600 are unidirected, meaning if $(i, j) \in \mathcal{E}$ then $(j, i) \in \mathcal{E}$. Furthermore, denote the neighbors
 601 of the i -th element as $\mathcal{N}_i = \{j | (i, j) \in \mathcal{E}\}$. Lastly, for the ease of notation, introduce two
 602 special indices: T for the boundary of an element that overlaps with the Dirichlet boundary
 603 condition, and similarly q for the Neumann boundary condition.

604 A.1.2 Weak Form of Discontinuous Galerkin Method

605 Choosing appropriate basis functions ϕ_k and ϕ_l and using the Interior Penalty Galerkin
 606 (IPG) scheme [5], the variational bilinear form for eq. (1a) is,

$$\sum_{i=1}^M a_{\epsilon,i}(\phi_k, \phi_l) = \sum_{i=1}^M L_i(\phi_k) \quad (52)$$

607 where ϵ is an user-specified parameter and,

$$a_{\epsilon,i}(\phi_k, \phi_l) = \int_{E^{(i)}} \left(\rho c_p \phi_k \frac{\partial \phi_l}{\partial t} + \nabla \phi_k \cdot (\mathbf{k} \nabla \phi_l) - \rho c_p \phi_k \mathbf{v} \cdot \nabla \phi_l \right) dE^{(i)} \quad (53a)$$

$$\begin{aligned} &= - \sum_{j \in \mathcal{N}_i \cup \{T_b\}} \int_{e_{ij}} \{ \mathbf{k} \nabla \phi_k \cdot n \} [\phi_l] de_{ij} + \epsilon \sum_{j \in \mathcal{N}_i \cup \{T_b\}} \int_{e_{ij}} \{ \mathbf{k} \nabla \phi_l \cdot n \} [\phi_k] de_{ij} \\ &\quad + \sigma \sum_{j \in \mathcal{N}_i \cup \{T_b\}} \int_{e_{ij}} [\phi_k] [\phi_l] de_{ij} \end{aligned} \quad (53b)$$

$$L_i(v) = \epsilon \sum_{j \in \mathcal{N}_i \cup \{T_b\}} \int_{e_{ij}} (\mathbf{k} \nabla \phi_l \cdot n) T_b de_{ij} + \int_{e_{iq}} \phi_k q_b de_{iq} + \sigma \int_{e_{iT}} \phi_k T_b de_{iT} \quad (53c)$$

608 In the bi-linear form above, the notations $[]$ and $\{ \}$ are respectively the jumps and averages
609 at the boundary e_{ij} share by two elements E_i and E_j ,

$$[u] = u|_{E_i} - u|_{E_j}, \quad \{u\} = \frac{1}{2} \left(u|_{E_i} + u|_{E_j} \right), \quad \text{for } x \in e_{ij} = E_i \cap E_j$$

610 Furthermore, in the bi-linear form, the terms associated with σ are introduced to enforce
611 the Dirichlet boundary conditions; σ is a penalty factor whose value can depend on the size
612 of an element. Depending on the choice of ϵ , the bi-linear form corresponds to symmetric
613 IPG ($\epsilon = -1$), non-symmetric IPG ($\epsilon = 1$), and incomplete IPG ($\epsilon = 0$). All these schemes
614 are consistent with the original PDE and have similar convergence rate with respect to mesh
615 size. In the following derivations, the case $\epsilon = 0$ is chosen for the sake of simplicity.

616 A.1.3 Discontinuous Galerkin Model

617 Next, the DG-based model is written in an element-wise form. For the i -th element, use a
618 set of P trial functions to represent the temperature as in eq. (6). Without loss of generality,
619 the trial functions are assumed to be orthogonal, so that,

$$\int_{E_i} \phi_l^i(x) \phi_k^i(x) d\Omega = 0, \quad l \neq k$$

620 where $|E_i|$ is the area ($n_d = 2$) or volume ($n_d = 3$) of the i -th element, and δ_{lk} is the Kronecker
621 delta function. Furthermore, for simplicity, choose $\phi_1^i = 1$. Thus, by orthogonality,

$$\int_{E_i} \phi_1^i(x) d\Omega = |E_i|, \quad \int_{E_i} \phi_k^i(x) d\Omega = 0, \quad k = 2, 3, \dots, P$$

622 Under the choice of basis functions, u_1^i is simply the average temperature of element E_i ,
623 denoted as \bar{u}_i .

624 Using test functions same as trial functions, the dynamics $\mathbf{u}^{(i)}$ is obtained by evaluating
625 the element-wise bi-linear forms,

$$a_{\epsilon,i}(\phi_k^{(i)}, T^{(i)}) = L_i(\phi_k^{(i)}), \quad k = 1, 2, \dots, P \quad (54)$$

626 Therefore, by standard variational principles, e.g., [5], the element-wise governing equation
627 is denoted as,

$$\mathbf{A}_i \dot{\mathbf{u}}_i = (\mathbf{B}_i + \mathbf{C}_i) \mathbf{u}_i + \sum_{j \in \mathcal{N}_i \cup \{T_b\}} (\mathbf{B}_{ij}^i \mathbf{u}_i + \mathbf{B}_{ij}^j \mathbf{u}_j) + \mathbf{f}_i(t), \quad \text{for } i = 1, 2, \dots, M \quad (55)$$

628 where for $k, l = 1, 2, \dots, P$,

$$[\mathbf{A}^{(i)}]_{kl} = \int_{E^{(i)}} \rho c_p \phi_k^{(i)} \phi_l^{(i)} dE^{(i)} \quad (56a)$$

$$[\mathbf{B}^{(i)}]_{kl} = - \int_{E^{(i)}} (\nabla \phi_k^{(i)}) \cdot (\mathbf{k} \nabla \phi_l^{(i)}) dE^{(i)} \quad (56b)$$

$$[\mathbf{C}^{(i)}]_{kl} = \int_{E^{(i)}} \rho c_p \phi_k^{(i)} \mathbf{v}^{(i)} \cdot \nabla \phi_l^{(i)} dE^{(i)} \quad (56c)$$

$$[\mathbf{B}_{ij}^{(i)}] = \int_{e_{ij}} \left\{ \mathbf{k} \nabla \phi_k^{(i)} \cdot \hat{n} \right\} \phi_l^{(i)} - \sigma [\phi_k^{(i)}] \phi_l^{(i)} de_{ij} \quad (56d)$$

$$[\mathbf{B}_{ij}^{(j)}] = \int_{e_{ij}} - \left\{ \mathbf{k} \nabla \phi_k^{(i)} \cdot \hat{n} \right\} \phi_l^{(j)} + \sigma [\phi_k^{(i)}] \phi_l^{(j)} de_{ij} \quad (56e)$$

$$[\mathbf{f}^{(i)}]_k = \int_{e_{iq}} \phi_k^{(i)} q_b de_{iq} + \sigma \int_{e_{iT}} \phi_k^{(i)} de_{iT} \quad (56f)$$

629 The matrices $\mathbf{A}^{(i)} \in \mathbb{R}^{P \times P}$, $\mathbf{B}^{(i)} \in \mathbb{R}^{P \times P}$, and $\mathbf{C}^{(i)} \in \mathbb{R}^{P \times P}$ are respectively the capacitance,
630 conductivity, and advection matrices for element i . These matrices depend on ρ , c_p , \mathbf{k} , and
631 \mathbf{v} , and hence can be non-linear functions of $\mathbf{u}^{(i)}$. Since the trial functions are orthogonal, if
632 ρc_p is constant within an element, $\mathbf{A}^{(i)}$ is diagonal; otherwise, \mathbf{A}_i is symmetric and positive
633 definite as $\rho c_p > 0$.

634 For compactness, the element-wise model in eq. (55) is also written in matrix form,

$$\mathbf{A} \dot{\mathbf{u}} = [\mathbf{B} + \mathbf{C}(\mathbf{u})] \mathbf{u} + \mathbf{f}(t) \quad (57)$$

635 where $\mathbf{u} = [\mathbf{u}^{(1)}, \mathbf{u}^{(2)}, \dots, \mathbf{u}^{(M)}]^T \in \mathbb{R}^{MP}$ includes all DG variables, $\mathbf{f} = [\mathbf{f}^{(1)}, \mathbf{f}^{(2)}, \dots, \mathbf{f}^{(M)}]^T \in$
636 \mathbb{R}^{MP} , \mathbf{A} and \mathbf{C} are matrices of M diagonal blocks whose i -th blocks are $\mathbf{A}^{(i)}$ and $\mathbf{C}^{(i)}$, and
637 \mathbf{B} is a matrix of $M \times M$ blocks whose (i, j) -th block is,

$$\mathbf{B}_{ij} = \begin{cases} \mathbf{B}^{(i)} + \sum_{j \in \mathcal{N}_i \cup \{T_b\}} \mathbf{B}_{ij}^{(i)}, & i = j \\ \mathbf{B}_{ij}^{(j)}, & i \neq j \end{cases} \quad (58)$$

638 The dependency of \mathbf{C} on \mathbf{u} is explicitly noted in eq. (57), which is the main source of non-
639 linearity in the current TPS problem. Moreover, the mesh velocity \mathbf{v} varies with space
640 and time, and thus the advection matrix \mathbf{C} varies with time as a function of the surface
641 temperature $T_q(x, t)$.

642 A.2 Coarse-Graining of Dynamics

643 The LCM is obtained by coarse-graining the full-order DG-FEM. This coarse-graining procedure produces resolved $\mathbf{r}^{(1)}(\mathbf{u}, t)$ and residual $\mathbf{r}^{(2)}(\mathbf{u}, t)$ dynamics as in eq. (24). This section
644 presents the detail derivations and magnitude analysis for the resolved and residual dynamics.
645

647 A.2.1 Resolved Dynamics

648 Using eq. (21), the resolved dynamics is computed as follows,

$$\mathbf{r}^{(1)}(\mathbf{u}, t) = \mathcal{P} [\Phi^+ \mathbf{A}(\mathbf{u})^{-1} (\mathbf{B}(\mathbf{u})\mathbf{u} + \mathbf{C}(\mathbf{u})\mathbf{u} + \mathbf{f}(t))] \quad (59a)$$

$$\begin{aligned} &= \Phi^+ \mathbf{A}(\mathbf{Pu})^{-1} \mathbf{PB}(\mathbf{Pu}) \mathbf{Pu} + \Phi^+ \mathbf{A}(\mathbf{Pu})^{-1} \mathbf{PC}(\mathbf{Pu}) \mathbf{Pu} \\ &\quad + \Phi^+ \mathbf{A}(\mathbf{Pu})^{-1} \mathbf{Pf}(t, \mathbf{Pu}) \end{aligned} \quad (59b)$$

$$\begin{aligned} &= \underbrace{\Phi^+ \mathbf{A}(\Phi \bar{\mathbf{u}})^{-1} \Phi}_{\#1} \underbrace{\Phi^+ \mathbf{B}(\Phi \bar{\mathbf{u}}) \Phi \bar{\mathbf{u}}}_{\#2} + \Phi^+ \mathbf{A}(\Phi \bar{\mathbf{u}})^{-1} \underbrace{\Phi \Phi^+ \mathbf{C}(\Phi \bar{\mathbf{u}}) \Phi \bar{\mathbf{u}}}_{\#3} \\ &\quad + \Phi^+ \mathbf{A}(\Phi \bar{\mathbf{u}})^{-1} \underbrace{\Phi \Phi^+ \mathbf{f}(t, \Phi \bar{\mathbf{u}})}_{\#4} \end{aligned} \quad (59c)$$

649 Detailed derivations for the #1, #2, and #4 terms can be found in Ref. [17]. The effects of
650 coarse-graining on the advection term #3 are analyzed next.

651 **Term #3** The $\mathbf{C}(\mathbf{u}) \in \mathbb{R}^{MP \times MP}$ matrix contains M diagonal of size $P \times P$, since the
652 basis functions are defined locally on each element. Therefore, $[\mathbf{C}(\mathbf{u})]_{ij} = \mathbf{0}$ for all $i \neq j$ with
653 $i, j = 1, 2, \dots, M$. It follows that for $k, l = 1, 2, \dots, N$,

$$[\Phi^+ \mathbf{C}(t, \Phi \bar{\mathbf{u}}) \Phi]_{kl} = \sum_{i=1}^M \sum_{j=1}^M \boldsymbol{\varphi}_i^{k+} [\mathbf{C}(t, \Phi \bar{\mathbf{u}})]_{ij} \boldsymbol{\varphi}_j^l \quad (60a)$$

$$= \sum_{i=1}^M \boldsymbol{\varphi}_i^{k+} [\mathbf{C}(t, \Phi \bar{\mathbf{u}})]_{ii} \boldsymbol{\varphi}_i^l \quad (60b)$$

$$= \sum_{i \in \mathcal{V}_k} \boldsymbol{\varphi}_i^{k+} [\mathbf{C}(t, \Phi \bar{\mathbf{u}})]_{ii} \boldsymbol{\varphi}_i^l \quad (60c)$$

654 where in the second row, the fact that $[\mathbf{C}(\mathbf{u})]_{ij} = 0$ for all $i \neq j$ is used, and in the last row,
655 the fact that $\boldsymbol{\varphi}_i^{k+} = 0$ for all $i \notin \mathcal{V}_k$ is used. Now, considering that $[\mathbf{C}(\mathbf{u})]_{ii}$ has a (1, 1)-th
656 zero element, i.e., $[C_{11}(t, \Phi \bar{\mathbf{u}})]_{ii} = 0$, and that if $k \neq l$ then $i \notin \mathcal{V}_l$ and thus $\boldsymbol{\varphi}_i^l = \mathbf{0}$, it follows
657 that for some index $i \in \mathcal{V}_k$,

$$\boldsymbol{\varphi}_i^{k+} [\mathbf{C}(t, \Phi \bar{\mathbf{u}})]_{ii} \boldsymbol{\varphi}_i^l = \boldsymbol{\varphi}_i^{k+} [\mathbf{C}(t, \Phi \bar{\mathbf{u}})]_{ii} \boldsymbol{\varphi}_i^k = \frac{|E_i|}{|\Omega_k|} [C_{11}(t, \Phi \bar{\mathbf{u}})]_{ii} = 0 \quad (61)$$

658 The matrix $[\Phi^+ \mathbf{C}(t, \Phi \bar{\mathbf{u}}) \Phi]_{kl} = 0$ for all $k, l = 1, 2, \dots, N$, and thus,

$$\bar{\mathbf{C}}(t, \bar{\mathbf{u}}) = \Phi^+ \mathbf{C}(t, \Phi \bar{\mathbf{u}}) \Phi = \mathbf{0} \quad (62)$$

659 as indicated by the LCM in eq. (10).

660 A.2.2 Magnitude Analysis for Residual Dynamics

661 Next, the magnitude of the residual dynamics $\mathbf{r}^{(2)}(\mathbf{u}, t)$ is analyzed to pinpoint the missing
662 physics in the LCM. By definition,

$$\mathbf{r}^{(2)}(\mathbf{u}, t) = \dot{\bar{\mathbf{u}}} - \mathbf{r}^{(1)}(\bar{\mathbf{u}}, t) \quad (63a)$$

$$= \Phi^+ \mathbf{r}(\mathbf{u}, t) - \mathbf{r}^{(1)}(\mathbf{u}, t) \quad (63b)$$

$$\begin{aligned} &= \underbrace{\Phi^+ \mathbf{A}(\mathbf{u})^{-1} \mathbf{B}(\mathbf{u}) \mathbf{u} - \bar{\mathbf{A}}(\bar{\mathbf{u}})^{-1} \bar{\mathbf{B}}(\bar{\mathbf{u}}) \bar{\mathbf{u}}}_{\#1} + \underbrace{\Phi^+ \mathbf{A}(\mathbf{u})^{-1} \mathbf{C}(\mathbf{u}) \mathbf{u} - \bar{\mathbf{A}}(\bar{\mathbf{u}})^{-1} \bar{\mathbf{C}}(t, \bar{\mathbf{u}}) \bar{\mathbf{u}}}_{\#2} \\ &\quad + \underbrace{\Phi^+ \mathbf{A}(\mathbf{u})^{-1} \mathbf{f}(t) - \bar{\mathbf{A}}(\bar{\mathbf{u}})^{-1} \bar{\mathbf{f}}(t)}_{\#3} \end{aligned} \quad (63c)$$

663 The magnitude analysis for terms $\#1$ and $\#3$ can be found in Ref. [17]. The analysis for
664 term $\#2$ is presented next. Let $\mathbf{D}(\bar{\mathbf{u}}) = \mathbf{A}(\Phi \bar{\mathbf{u}})^{-1} \mathbf{P} \mathbf{C}(t, \Phi \bar{\mathbf{u}})$, then,

$$\Phi^+ \mathbf{A}(\mathbf{u})^{-1} \mathbf{C}(\mathbf{u}) \mathbf{u} - \bar{\mathbf{A}}(\bar{\mathbf{u}})^{-1} \bar{\mathbf{C}}(t, \bar{\mathbf{u}}) \bar{\mathbf{u}} \quad (64a)$$

$$= \Phi^+ \mathbf{A}(\mathbf{u})^{-1} \mathbf{C}(\mathbf{u}) \mathbf{u} - \Phi^+ \mathbf{A}(\Phi \bar{\mathbf{u}})^{-1} \mathbf{P} \mathbf{C}(t, \Phi \bar{\mathbf{u}}) \Phi \Phi^+ \mathbf{u} \quad (64b)$$

$$= \Phi^+ \mathbf{A}^{-1}(\mathbf{u}) \mathbf{C}(\mathbf{u}) \mathbf{u} - \Phi^+ \mathbf{D}(\bar{\mathbf{u}}) \Phi \Phi^+ \mathbf{u} \quad (64c)$$

$$(64d)$$

665 where $\mathbf{P} = \Phi \Phi^+$. Thus,

$$\|\Phi^+ \mathbf{A}(\mathbf{u})^{-1} \mathbf{C}(\mathbf{u}) \mathbf{u} - \bar{\mathbf{A}}(\bar{\mathbf{u}})^{-1} \bar{\mathbf{C}}(t, \bar{\mathbf{u}}) \bar{\mathbf{u}}\| \quad (65a)$$

$$\leq \|\Phi^+ \mathbf{A}^{-1}(\mathbf{u}) \mathbf{C}(\mathbf{u}) \mathbf{u} - \Phi^+ \mathbf{D}(\bar{\mathbf{u}}) \mathbf{u}\| + \|\Phi^+ \mathbf{D}(\bar{\mathbf{u}}) \mathbf{u} - \Phi^+ \mathbf{D}(\bar{\mathbf{u}}) \Phi \Phi^+ \mathbf{u}\| \quad (65b)$$

$$\leq \|\Phi^+ \| \underbrace{\|\mathbf{A}^{-1}(\mathbf{u}) \mathbf{C}(\mathbf{u}) \mathbf{u} - \mathbf{D}(\bar{\mathbf{u}}) \mathbf{u}\|}_{\#1} + \|\Phi^+ \mathbf{D}(\bar{\mathbf{u}})\| \underbrace{\|\mathbf{u} - \Phi \Phi^+ \mathbf{u}\|}_{\#2} \quad (65c)$$

666 where term $\#2$ is due to the approximation of non-uniform temperature as constants, and
667 term $\#1$ is the error in the advection dynamics due to coarse-graining.

668 A.3 Lumped Capacitance Model

669 The following assumptions are employed: (1) the temperature in component (i) is described
670 by a scalar time-varying average temperature $\bar{u}^{(i)}$, (2) between neighboring components (i)

and (j) the heat flux is approximated as,

$$q_{ij} = \frac{\bar{u}^{(j)} - \bar{u}^{(i)}}{R_{ij}} \quad (66)$$

where R_{ij} is the thermal resistance. Empirically, for a component of isotropic heat conductivity k , length ℓ , and cross-section area A , the thermal resistance is $R = \ell/kA$. Between components i and j , define $R_{ij} = R_i + R_j$. In addition, the heat flux due to Dirichlet boundary condition is computed as $q_{iT} = (T_b - \bar{u}^{(i)})/R_i$.

At component i , the dynamics of LCM are given by,

$$\int_{E^{(i)}} \rho c_p \dot{\bar{u}}^{(i)} dE^{(i)} = \left(\sum_{j \in \mathcal{N}_i} \int_{e_{ij}} \frac{\bar{u}^{(j)} - \bar{u}^{(i)}}{R_{ij}} de_{ij} \right) + \int_{e_{iq}} q_b de_{iq} + \int_{e_{iT}} \frac{T_b - \bar{u}^{(i)}}{R_i} de_{iT} \quad (67a)$$

$$\bar{A}^{(i)} \dot{\bar{u}}^{(i)} = \left(\sum_{j \in \mathcal{N}_i} \frac{|e_{ij}|}{R_{ij}} (\bar{u}^{(j)} - \bar{u}^{(i)}) \right) + |e_{iq}| \bar{q}^{(i)} + \frac{|e_{iT}|}{R_i} (\bar{T}^{(i)} - \bar{u}^{(i)}) \quad (67b)$$

$$= \sum_{j \in \mathcal{N}_i} \left(-\frac{|e_{ij}|}{R_{ij}} \bar{u}^{(i)} + \frac{|e_{ij}|}{R_{ij}} \bar{u}^{(j)} \right) + \left(-\frac{|e_{iT}|}{R_i} \bar{u}^{(i)} \right) + \left(|e_{iq}| \bar{q}^{(i)} + \frac{|e_{iT}|}{R_i} \bar{T}^{(i)} \right) \quad (67c)$$

$$= \sum_{j \in \mathcal{N}_i \cup \{T_b\}} \left(\bar{B}_{ij}^{(i)} \bar{u}^{(i)} + \bar{B}_{ij}^{(j)} \bar{u}^{(j)} \right) + \bar{f}^{(i)} \quad (67d)$$

where in eq. (67b) $|e|$ denotes the length ($d = 2$) or area ($d = 3$) of a component boundary e . The $\bar{A}^{(i)}$, $\bar{B}_{ij}^{(i)}$, and $\bar{B}_{ij}^{(j)}$ quantities are provided in eq. (13).

The lumped-mass representation for the four-component TPS is shown in Fig. ???. Let v_i represent the area of the i -th element, $\overline{\rho c_{p,i}}$, the heat capacity evaluated using the average temperature $\bar{u}^{(i)}$, and $1/R_{ij} = 1/R_i(\bar{u}^{(i)}) + 1/R_j(\bar{u}^{(j)})$ the equivalent thermal resistance between elements i and j . Leveraging the formulas from eqs. (12) and (13), the LCM matrices are given by,

$$\bar{\mathbf{A}} = \begin{bmatrix} \overline{\rho c_{p,1}} v_1 & 0 & 0 & 0 \\ 0 & \overline{\rho c_{p,2}} v_2 & 0 & 0 \\ 0 & 0 & \overline{\rho c_{p,3}} v_3 & 0 \\ 0 & 0 & 0 & \overline{\rho c_{p,4}} v_4 \end{bmatrix}, \quad (68a)$$

$$\bar{\mathbf{B}} = \begin{bmatrix} \frac{1}{R_{12}} + \frac{1}{R_{14}} & -\frac{1}{R_{12}} & 0 & -\frac{1}{R_{14}} \\ -\frac{1}{R_{12}} & \frac{1}{R_{12}} + \frac{1}{R_{24}} + \frac{1}{R_{23}} & -\frac{1}{R_{23}} & -\frac{1}{R_{24}} \\ 0 & -\frac{1}{R_{32}} & \frac{1}{R_{32}} + \frac{1}{R_{34}} & -\frac{1}{R_{34}} \\ -\frac{1}{R_{14}} & -\frac{1}{R_{24}} & -\frac{1}{R_{34}} & \frac{1}{R_{14}} + \frac{1}{R_{24}} + \frac{1}{R_{34}} \end{bmatrix}, \quad \bar{\mathbf{f}} = \begin{bmatrix} \bar{q}^{(1)} \\ \bar{q}^{(2)} \\ \bar{q}^{(3)} \\ 0 \end{bmatrix} \quad (68b)$$

References

- [1] Adam J. Amar, A. Brandon Oliver, Benjamin S. Kirk, Giovanni Salazar, and Justin Drob. Overview of the charring ablator response (char) code. In AIAA, editor, *AIAA*

- 687 *Aviation Forum*, 2016.
- 688 [2] Guy L. Bergel, Frank B. Beckwith, Gabel J. de Frias, Kevin M. Manktelow, Mark T.
 689 Merewether, Scott T. Miller, Krishen J. Parmar, Timothy S. Shelton, Jesse T. Thomas,
 690 Jeremy T. Trageser, Benjamin T. Treweek, Michael V. Veilleux, and Ellen B. Wagman.
 691 *Sierra/SolidMechanics 5.6 User's Manual*, 2022.
- 692 [3] Ricky T. Q. Chen, Yulia Rubanova, Jesse Bettencourt, and David Duvenaud. Neural
 693 ordinary differential equations, 2019.
- 694 [4] Jonathan Clausen, Victor Brunini, Lincoln Collins, Robert C Knaus, Alec Kucala,
 695 Stephen Lin, Daniel Robert Moser, Malachi Phillips, Thomas Michael Ransegrenola,
 696 Samuel Ramirez Subia, et al. Sierra multimechanics module: Aria verification manual-
 697 version 5.22. Technical report, Sandia National Lab.(SNL-NM), Albuquerque, NM
 698 (United States), 2024.
- 699 [5] Gary Cohen and Sebastien Pernet. *Finite Element and Discontinuous Galerkin Methods*
 700 for Transient Wave Equations. Springer Dordrecht, Le Chesnay and Toulouse France,
 701 2018.
- 702 [6] Jianhao Fang, Weifei Hu, Zhenyu Liu, Yuhao Zhou, Chao Wei, and Jianrong Tan. A
 703 reduced order finite element-informed surrogate model for approximating global high-
 704 fidelity simulations. *Structural and Multidisciplinary Optimization*, 67(12), 2024.
- 705 [7] Matthew Gasch, Keith Peterson, Mairead Stackpoole, Ethiraj Venkatapathy, Gregory
 706 Gonzales, and Kyle Hendrickson. Development of advanced ablative carbon phenolic
 707 tps for future nasa missions and commercial space. In *38th Annual Small Satellite*
 708 *Conference*, Logan, Utah, May 2024.
- 709 [8] Micah A. Howard and Ben F. Blackwell. A multi-dimensional finite element based solver
 710 for decomposing and non-decomposing thermal protection systems. In AIAA, editor,
 711 *AIAA Aviation Forum*, 2015.
- 712 [9] Frank P. Incropera, David P. DeWitt, Theodore L. Bergman, and Adrienne S. Lavine.
 713 *Fundamentals of Heat and Mass Transfer*. Wiley, Hoboken, NJ, 7th edition, 2011.
- 714 [10] R. J. Klock and Carlos Cesnik. Nonlinear thermal reduced-order modeling for hypersonic
 715 vehicles. *AIAA Journal*, 55(7), 2017.
- 716 [11] Arun Govind Neelan. Linear and non-linear reduced order model of scramjet. In *Advances*
 717 *in Multidisciplinary Design, Analysis and Optimization*, pages 111–118, Singapore,
 718 2025.
- 719 [12] Alberto Padovan, Blaine Vollmer, Francesco Panerai, Marco Panesi, Kelly A. Stephani,
 720 and Daniel J. Bodony. An extended bformulation for ablating-surface boundary condi-
 721 tions. *International Journal of Heat and Mass Transfer*, 218:124770, 2024.
- 722 [13] Eric Parish and Karthik Duraisamy. Non-markovian closure models for large eddy
 723 simulations using the mori-zwanzig formalism. *Phys. Rev. Fluids*, 2:014604, Jan 2017.

- 724 [14] Eric Parish and Karthik Duraisamy. A unified framework for multiscale modeling using
725 the mori-zwanzig formalism and the variational multiscale method. *ArXiv*, 12 2017.
- 726 [15] Eric Parish and Karthik Duraisamy. *Coarse-Graining Turbulence Using the*
727 *Mori-Zwanzig Formalism*. Cambridge University Press, Cambridge, 2025.
- 728 [16] Adam Thelen, Xiaoge Zhang, Olga Fink, Yan Lu, Sayan Ghosh, Byeng D. Youn,
729 Michael D. Todd, Sankaran Mahadean, Chao Hu, and Zhen Hu. A comprehensive
730 review of digital twin – part 1: modeling and twinning enabling technologies. *Structural*
731 *and Multidisciplinary Optimization*, 65(12), 2022.
- 732 [17] Carlos A. Vargas Venegas, Daning Huang, Patrick Blonigan, and JohnTencer. Physics-
733 infused reduced-order modeling for analysis of multi-layered hypersonic thermal protec-
734 tion systems, 2025.
- 735 [18] Yongyong Xian, Baisong Pan, and Luping Luo. A new model updating strategy with
736 physics-based and data-driven models. *Structural and Multidisciplinary Optimization*,
737 64(1), 2021.
- 738 [19] Yin Yu, John Harlim, Daning Huang, and Yan Li. Learning coarse-grained dynamics
739 on graph. *arXiv preprint arXiv:2405.09324*, 2024.